Semimicroscopic nucleon-nucleus spherical optical model for nuclei with $A \geqslant 40$ at energies up to 200 MeV

E. Bauge, J. P. Delaroche, and M. Girod
Commissariat à l'Energie Atomique, Service de Physique Nucléaire, Boite Postale 12, 91680 Bruyères-le-Châtel, France
(Received 21 January 1998)

A nucleon-nucleus optical model potential (OMP) is built from the nuclear matter (NM) approach of Jeukenne, Lejeune, and Mahaux (JLM). The imaginary component of the on-shell NM mass operator, originally parametrized by these authors as a function of matter density and energy, is given a new representation suitable for energies from 1 to 200 MeV. The JLM model extended in this manner is then applied through an improved local density approximation (LDA) to treat nucleon scattering from closed- and near closed-shell nuclei with masses $40 \leqslant A \leqslant 209$. For proton, neutron, and charge radial densities, we use those obtained from Hartree-Fock-Bogoliubov calculations based on the finite range, density dependent Gogny force. Several LDA and spin-orbit potential prescriptions are tested to select those which provide the best overall description of elastic scattering and reaction measurements. Over three hundred datasets including differential cross sections, analyzing powers, spin rotation functions, and reaction cross sections are considered in the present analyses. The OMP components include normalization factors which are optimized for each incident energy, probe, and for most target nuclei. We give close forms which represent the energy variation of these factors for the $n+X$ and $p+X$ systems. The global OMPs built in this manner produce a good overall description of the neutron and proton scattering and reaction measurements available up to 200 MeV. [S0556-2813(98)05208-X]

PACS number(s): 24.10.Ht, 25.40.Cm, 25.40.Dn, 25.60.Dz

I. INTRODUCTION

During the past thirty years a considerable effort has been put on establishing the nucleon-nucleus optical model potential (OMP) on microscopic grounds, that is describing nucleon scattering in terms of an elementary process modified by the presence of the nuclear medium. Milestones on this path are offered in the proceedings of the 1978 Hamburg and 1982 Bloomington conferences [1,2]. Medium effects on the NN interaction can be tackled in many ways which, for convenience, we classify into two broad categories. The first one includes relativistic mean-field models, while the second one deals with nonrelativistic theories of the many body problem.

Among the latter approaches, those based on the Brueckner-Hartree-Fock (BHF) theory of nuclear matter (NM) have played a key role in the development of microscopic OMPs and effective NN interactions at low and medium energies [2–4]. Briefly this derivation proceeds as follows. From BHF calculations in nuclear matter, a mass operator M is first deduced, which is a function of the nuclear medium density ρ, the nucleon momentum k, and the energy E. A local OMP in nuclear matter is obtained by evaluating M on the energy shell. This potential is then given a form usable for OMP calculations by performing a local density approximation (LDA). Jeukenne, Lejeune, and Mahaux have thoroughly developed this NM based OMP, and provided a simple parametrization of their on-shell nuclear matter results in terms of ρ and E up to 160 MeV. Once implemented with an improved LDA this OMP representation defines the JLM model [5,6]. This accomplishment has marked the beginning of many investigations regarding the predictive power of the JLM model in neutron and proton scattering studies. So far, this model has been tested up to 160 MeV against the volume integrals and root mean square radii of phenomenological real and imaginary central potentials, as well as against differential scattering cross sections and analyzing powers measured at selected incident energies below 80 MeV. Quite good fits to the experimental data are obtained through empirical normalizations of the JLM potential depths [7–11].

Many other OMP calculations performed using the nonrelativistic theory of nuclear matter have also been tested up to 500 MeV, in which standard folding [12–19] as well as full-folding potentials [20–24] are considered. In the meantime, Kelly *et al.* [25,26] have developed a phenomenological effective interaction inspired from, and guided by theory to assess the validity of the local density assumption on which these scattering models are based.

The local density concept, a central issue in microscopic OMP studies, is here revisited through large scale nucleon scattering and reaction analyses conducted exclusively in the JLM model context over the 1 to 200 MeV and $40 \leqslant A \leqslant 209$ ranges.

If implemented with a robust LDA, this easy to handle model (the exchange potential components are explicitly treated at the BHF level) would display appealing properties, which would make it ideally suited for many applications, including those related to the design of accelerator-driven systems [27,28]. In this respect, because of its solid theoretical foundations, we may reasonably hope that this model will produce reliable predictions, even in cases where no experimental data is available.

At this point, we would like to acknowledge that another large scale OMP study has been conducted recently by Clark *et al.* [29,30]. In this work, the authors have succeeded in establishing a phenomenological, global Dirac potential for protons scattered from ^{12}C, ^{16}O, ^{40}Ca, ^{90}Zr, and ^{208}Pb in the

20 to 1040 MeV range. The fits obtained are of high quality, especially those pertinent to analyzing power and spin rotation functions. This success met at 500 MeV is mostly due to the complex spin-orbit potential which occurs naturally in the Dirac equation. In contrast, the standard phenomenological Schrödinger OMP fails in the intermediate energy region ($E>200$ MeV). The comparative success of the Dirac phenomenology, attributed to its relativistic formulation, has stimulated the development of relativistic mean field theories which are presently challenged in neutron-nucleus reactions [31–36]. Note that the validity ranges of the Dirac phenomenology and that of our model overlap between 20 and 200 MeV.

This paper is organized as follows. In Sec. II, we offer a brief presentation of the JLM model and establish our notations. The original close forms assigned to the JLM results obtained in nuclear matter up to 160 MeV are then extended to allow for JLM model calculations between 160 and 200 MeV, an energy interval where a wealth of scattering data is available. Several LDA and spin-orbit (SO) prescriptions to be tested in actual OMP calculations performed using Hartree-Fock-Bogoliubov nuclear radial densities, are presented in Sec. III. Detailed spherical optical model analyses are described in Sec. IV for neutrons and protons incident on ^{40}Ca, ^{54,56}Fe, ^{58,60}Ni, ^{63,65}Cu, ^{90}Zr, ^{93}Nb, ^{116,120}Sn, ^{208}Pb, and ^{209}Bi, which help fixing the best overall LDA and SO potential prescriptions as well as normalization factors attached to the potential depths. These factors are given close forms in Sec. V, and discussed separately for incident protons and neutrons. Global neutron and protons OMPs are thus obtained. Their predictive power is challenged in Sec. VI through comparisons with various scattering and reaction measurements.

II. OMP IN NUCLEAR MATTER

A. Microscopic optical potential

Let us first remind the reader of the notations, which were originally defined in [5,6,37]. In infinite nuclear matter, the optical model potential is closely related to the mass operator M [38] which depends on the momentum k and the energy E. In principle $M(k,E)$ may be calculated from the reaction matrix g defined by [3,5,6]

$$g_\rho(w)=v+\sum_{\vec{a}>k_F,\vec{b}>k_F} v\,\frac{|\vec{a},\vec{b}\rangle\langle\vec{a},\vec{b}|}{w-e(a)-e(b)-i\delta}g_\rho(w), \tag{1}$$

where v is the bare nucleon-nucleon interaction. The index ρ is meant to emphasize the fact that the g-matrix is density dependent, a property rooted in the Pauli blocking operator present in the right hand side of Eq. (1). The density ρ is related to the Fermi momentum k_F by $\rho=2/(3\pi^2)k_F^3$, and e defined as

$$e(a)=a^2/2m+U(a), \tag{2}$$

where m is the nucleon mass, and U an auxiliary potential.

This problem cannot be solved exactly. However Jeukenne, Lejeune, and Mahaux have shown [6] how to calculate the mass operator from the g-matrix, using Reid's hard core interaction [39] as the bare NN force in the Brueckner-Hartree-Fock approximation (BHF) [40]. In this context, $M\approx M_\rho^{(1)}$ is made of two components and expressed as

$$M_\rho^{(1)}=M_\rho^{(0)}+\delta M_\rho^{(1)}, \tag{3}$$

where $M_\rho^{(0)}$ is the mass operator in symmetric nuclear matter, and $\delta M_\rho^{(1)}$ is the first order term of a development in terms of $\Omega=1/2(k_{F_n}-k_{F_p})$ around $M_\rho^{(0)}$ [37], k_{F_n} and k_{F_p} being the Fermi momenta of the neutron and proton distributions, respectively. After evaluating $M_\rho^{(1)}$ on the energy shell, the optical potential is written as [37]

$$U_{\rm NM}(\rho,E)=V_0(\rho,E)+\alpha\tau V_1(\rho,E)+i[W_0(\rho,E)+\alpha\tau W_1(\rho,E)], \tag{4}$$

where $\alpha=(\rho_n-\rho_p)/(\rho_n+\rho_p)$ is the asymmetry term, τ is $+1$ for proton and -1 for neutron projectiles, and where V_0, V_1, W_0, and W_1 are potential components defined through

$$V_0(\rho,E)={\rm Re}M_\rho^{(0)}(k(E),E), \tag{5}$$

$$V_1(\rho,E)=\frac{\tilde{m}}{m}{\rm Re}N_\rho(k(E),E), \tag{6}$$

$$W_0(\rho,E)=\frac{m}{\bar{m}}{\rm Im}M_\rho^{(0)}(k(E),E), \tag{7}$$

and

$$W_1(\rho,E)=\frac{m}{\bar{m}}{\rm Im}N_\rho(k(E),E), \tag{8}$$

with

$$N_\rho(k,E)=\frac{1}{\alpha}\delta M_\rho^{(1)}. \tag{9}$$

The quantities $\tilde{m}/m$ and $\bar{m}/m$ are, respectively, the k mass and the E mass representing the true nonlocality and the true energy dependence of the OMP [4]

$$\frac{m}{\tilde{m}}=1+\frac{m}{k}\frac{\partial}{\partial k}({\rm Re}M_\rho^{(0)})|_{k=k(E)}, \tag{10}$$

$$\frac{\bar{m}}{m}=1-\frac{\partial}{\partial E}({\rm Re}M_\rho^{(0)})|_{E=E}. \tag{11}$$

Also, according to the prescriptions in [41,42] the imaginary part of the OMP is then scaled by the effective mass $\tilde{m}/m$. These definitions are relevant to the neutron OMP. For incident protons, the current prescription is to evaluate the optical potential at $E-V_c$ [6].

B. Parametrization of the on-shell BHF results

In order to simplify the use of their OMP, JLM have parametrized $U_{\rm NM}(\rho,E)$ below 160 MeV as a sum of powers

of the density multiplied by powers of the projectile energy [37]. These forms are given below.

(i) The isoscalar part of the real OMP [37]

$$\mathrm{Re}(M_0(\rho,E))=\sum_{i,j=1}^{3} a_{ij}\rho^i E^{j-1}, \tag{12}$$

where E is expressed in MeV, ρ in fm^{-3}, and a_{ij} are coefficients given in [37].

(ii) The isovector part of the real OMP [37]

$$\mathrm{Re}(N(\rho,E))=\sum_{i,j=1}^{3} b_{ij}\rho^i E^{j-1}. \tag{13}$$

(iii) The isoscalar part of the imaginary OMP [37]

$$W_0(\rho,E)=\left[1+\frac{D}{(E-\epsilon_F)^2}\right]^{-1}\sum_{i,j=1}^{4} d_{ij}\rho^i E^{j-1}, \tag{14}$$

where ϵ_F is the Fermi energy, and $D=600$ MeV^2 if $E>10$ MeV [37], and $D=100$ MeV^2 if $E<10$ MeV [43].

(iv) The isovector part of the imaginary OMP [37]

$$\mathrm{Im}(N(\rho,E))=\left[1+\frac{F}{E-\epsilon_F}\right]^{-1}\sum_{i,j=1}^{4} f_{ij}\rho^i E^{j-1}, \tag{15}$$

where $F=1$ MeV. Here, ϵ_F is depending on the energy range. If $E>10$ MeV then ϵ_F is parametrized as [37]

$$\epsilon_F{}^h(\rho)=\rho(-510.8+3222\rho-6250\rho^2), \tag{16}$$

while for $E\leqslant 10$ MeV [43]

$$\epsilon_F{}^l(\rho)=-22.0-\rho(298.52-3760.23\rho+12345\rho^2). \tag{17}$$

(v) The k mass (10) [37]

$$\frac{\tilde{m}(\rho,E)}{m}=1-\sum_{i,j=1}^{3} c_{ij}\rho^i E^{j-1}, \tag{18}$$

and the E mass (11) calculated [37] using

$$\frac{m^*}{m}=\frac{\tilde{m}}{m}\cdot\frac{\overline{m}}{m}, \tag{19}$$

with

$$\frac{m^*(\rho,E)}{m}=1-\frac{d}{dE}V_0(\rho,E). \tag{20}$$

C. Limitations of the original JLM parametrization

The first obvious limitation of this original parametrization is the discontinuity of the imaginary potential at 10 MeV, that leads to a discontinuity in the volume integral J_w/A, and to a kink in the reaction cross section calculated in finite nuclei as a function of energy.

The second limitation is due to the energy range of the parametrization: if the imaginary OMP is evaluated above 160 MeV using the above parametrization, it exhibits a positive region at low density. Obviously this deficiency propagates into the imaginary OMP in finite nuclei. This feature is illustrated for neutrons incident on ^{208}Pb in the middle panel of Fig. 1 where the absorptive potential is positive at the nuclear surface as soon as $E>160$ MeV. This is clearly an artifact of the original parametrization of the BHF results by a sum of powers of E and ρ: such a fit does not lend itself very well to extrapolation. Thus, in order to evaluate the imaginary potential above 160 MeV, one has to find another way of extrapolating towards higher energies.

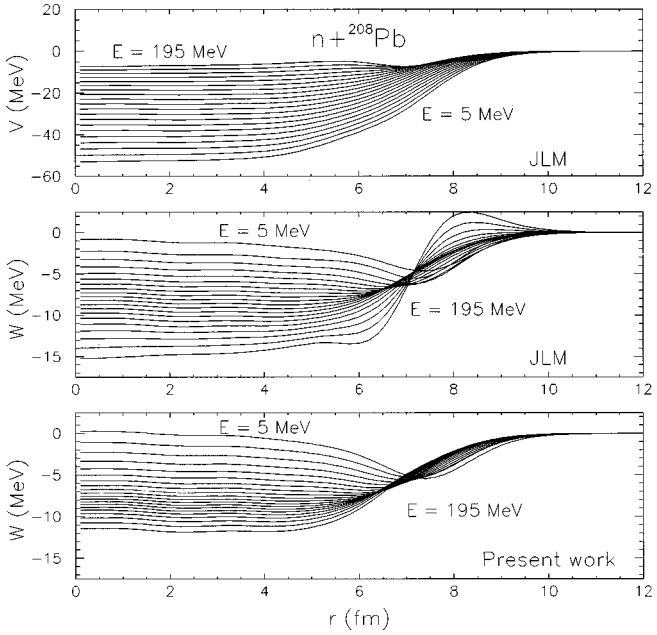

FIG. 1. The neutron OMP for ^{208}Pb calculated between 5 and 195 MeV using the JLM parametrization. The real part of the OMP is shown in the upper panel while the middle and lower panels hold the imaginary part of the OMP calculated using, respectively, the original JLM NM OMP parametrization or our improved NM OMP parametrization. The LDA (27) is used for this calculation.

D. New parametrization

Therefore, we have refitted the Im(M_0) and Im(N) potentials using the functional forms (14) and (15), obtaining new values for the d_{ij}, D, and f_{ij} coefficients. In this process, ϵ_F was taken as

$$\epsilon_F(\rho,E)=f(E)\epsilon_F{}^l(\rho)+(1-f(E))\epsilon_F{}^h(\rho), \tag{21}$$

where

$$f(E)=[1+\exp((E-E_0)/a_E)]^{-1}, \tag{22}$$

with $E_0=10$ MeV and $a_E=2$ MeV. Now, there is a smooth transition between the low and high energy behaviors of the Fermi energy parametrization.

Furthermore, we have put the following constraints on the fits.

(i) Between 0 and 10 MeV the target values for Im(M_0) and Im(N) were the values calculated with the low energy parametrization of Lejeune [43].

(ii) Between 18 and 130 MeV the target values for Im(M_0) and Im(N) were the values calculated with the parametrization of JLM [37].

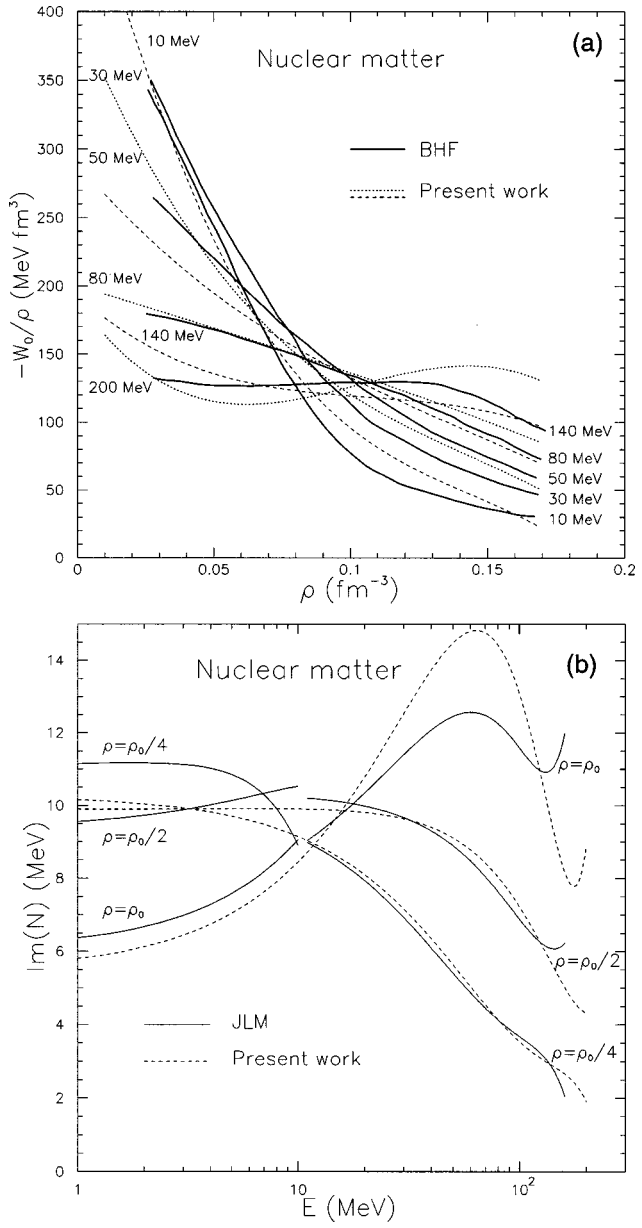

FIG. 2. (a) Comparison of the quantity $W_0(\rho,E)/\rho$ from [37] (solid and dotted lines) with the same quantity calculated with the new JLM OMP parametrization (dashed and dotted lines), at the energies 10, 30, 50, 80, and 140 MeV. (b) Comparison between energy dependences of the imaginary part of the isovector OMP Im(N), calculated using the original JLM parametrizations and the same quantity calculated with our reparametrization of the JLM OMP. This comparison is shown here for nuclear densities of ρ_0, $\rho_0/2$, and $\rho_0/4$.

(iii) Above 130 MeV, the target values for Im(M_0) and Im(N) were linearly extrapolated from their respective values [37] at 130 MeV.

It is important to note that the region between 9 and 19 MeV was left free of constraints so that the functions could ''heal.'' The fit was performed on 2500 points in (ρ,E) space. Figure 2(a) shows a comparison of the fitted values of W_0/ρ (dotted and dashed lines) with values of W_0/ρ from [37] (full line) at 10, 30, 50, 80, and 140 MeV. This figure shows that this fitted OMP component stays within 10% of the original values and that the overall evolutions of both $W_0(\rho,E)/\rho$ sets are similar. Note that the 10 MeV curve shown as a continuous line in Fig. 2(a) is from [37] whereas the values used as target values at 10 MeV were from [43], so there is nothing alarming about the difference between dashed and full lines at 10 MeV on this figure.

For Im(N) the same fitting procedure as for W_0 has been applied. Figure 2(b) shows Im(N) calculated for $\rho=\rho_0$, $\rho_0/2$, and $\rho_0/4$ as a function of energy ($\rho_0=0.17$ fm^{-3}). Both the new parametrization (dashed lines) and the old parametrization (full lines, from [37] above 10 MeV and from [43] below 10 MeV) are represented there. On this plot it can be seen that, while the fit is not perfect, the overall features of the original NM OMP are well reproduced by the present fit. The reader should also notice that the discontinuities of the original parametrization at 10 MeV are gone with the new parametrization.

The result of this fit is a new set of d_{ij}, D, and f_{ij} coefficients. The coefficients d_{ij} and D are shown in Table I, and the coefficients F_{ij} in Table II. When adopted in actual OMP calculations (see Sec. III), this new parametrization cures the deficiency of the imaginary OMP discussed above. The lower panel of Fig. 1 shows that the neutron absorption for ^{208}Pb is no longer positive at large radii for $E\geqslant 160$ MeV. As can be seen, the new imaginary OMP smoothly changes from surface to volume shape as E increases, the transition occurring at about 40 MeV. Also note that the original and new imaginary potential parametrizations produce rather different potential depths in finite nuclei (compare the middle and lower panels of Fig. 1). This difference will most likely propagate into the strength of the normalization factor λ_w (see Sec. IV) and affect the comparison with the λ_w's obtained in earlier scattering studies [8–11].

The upper panel of Fig. 1 also shows the real part of the neutron JLM potential calculated for ^{208}Pb up to 195 MeV. The radial distribution displays a volume shape, except at higher incident energies where it transforms into the sum of a surface and volume terms as expected [44].

The original JLM parametrization [37] provides rather weak real potential depths when extrapolated beyond 160 MeV. We have checked from sensitivity calculations that this OMP component plays a minor role in scattering observable predictions at 180 and 200 MeV incident energies. For all these reasons, the OMP analyses presented in this paper will be conducted using the new parametrization [i.e., Eqs. (21),(22) and Tables I and II] of the imaginary central potential, and the original parametrization [37] of Jeukenne, Lejeune, and Mahaux for the real central potential.

III. OMP IN FINITE NUCLEI

In this section we describe the other ingredients needed to run our OMP calculations, namely the local density approximation, spin-orbit interaction, and nucleon densities.

A. Local density approximation and improved LDA

The nuclear matter results discussed above cannot be directly applied to finite nuclei. A local density approximation can be used to make nuclear matter results relevant to finite nuclei. The LDA assigns the value of the OMP in nuclear matter evaluated for a density of $\rho(r)$ to the finite nucleus OMP at a distance r from the center of the nucleus [37]

TABLE I. Present coefficients d_{ij} with $D=625$ MeV^2 in the expression (14).

$i\backslash j$	1	2	3	4
1	$-0.6599\times10^{+3}$	$+0.1077\times10^{+2}$	-0.7886×10^{-1}	$+0.1875\times10^{-3}$
2	$+0.1144\times10^{+5}$	$-0.2908\times10^{+3}$	$+0.2443\times10^{+1}$	-0.6203×10^{-2}
3	$-0.7451\times10^{+5}$	$+0.2207\times10^{+4}$	$-0.1993\times10^{+2}$	$+0.5175\times10^{-1}$
4	$+0.1761\times10^{+6}$	$-0.5458\times10^{+4}$	$+0.5113\times10^{+2}$	$-0.1339\times10^{+0}$

$$U_{\mathrm{LDA}}(r,E)=U_{\mathrm{NM}}(\rho(r),E), \tag{23}$$

where U_{LDA} is the OMP in a finite nucleus, and U_{NM} is the optical potential in nuclear matter (4) calculated for the same neutron excess. While this approximation is able to reproduce well the volume integrals of phenomenological OMPs, it leads to underestimating their root mean square (rms) radii. The improved LDA has been introduced to cure this behavior by widening the rms radius with a Gaussian form factor [37], thus giving a finite range to the effective interaction. With this improved LDA, the OMP in finite nuclei reads

$$U_{\mathrm{ILDA}i}(r,E)=(t\sqrt{\pi})^{-3}\int \mathcal{U}_i(r,r',E) \times\exp(-|\vec{r}-\vec{r'}|^2/t_r^2)\rho(r')d\vec{r'}, \tag{24}$$

where $U_{\mathrm{ILDA}i}$ is the OMP calculated with the improved LDA prescription i, and t the range of the Gaussian. Three familiar prescriptions have been considered [8–11,45,46]

$$\mathcal{U}_p(r,r',E)=\frac{U_{\mathrm{NM}}(\rho(r),E)}{\rho(r)}, \tag{25}$$

$$\mathcal{U}_m(r,r',E)=\frac{U_{\mathrm{NM}}(\rho[(r+r')/2],E)}{\rho[(r+r')/2]}, \tag{26}$$

and

$$\mathcal{U}_t(r,r',E)=\frac{U_{\mathrm{NM}}(\rho(r'),E)}{\rho(r')}, \tag{27}$$

depending on whether the interaction is evaluated at the projectile (25), midpoint (26), or target position (27).

In previous studies [8,37,45], two different ranges (t_r and t_i) are considered, the first one for the real and the second one for the imaginary components of $U_{\mathrm{LDA}i}$. t_r and t_i are found to lay between 1 and 1.4 fm, which are commonly accepted values for effective interactions [47]. In Sec. V D we will estimate the values of t_r and t_i which provide the best overall agreement between the present OMP predictions and experimental data.

B. Spin-orbit potential

In order to faithfully reproduce experimental analyzing power [$A_y(\theta)$], spin rotation function [$Q(\theta)$ and $R(\theta)$], and differential scattering cross section [$\sigma(\theta)$] measurements, one needs not only a good central potential, but a good spin-orbit potential as well. Since no SO interaction is provided by the JLM model, we should rely on a specific prescription to treat this OMP component.

In previous works performed using the JLM OMP [8,48], the spin-orbit part of the M3Y interaction [49] has been successfully used. While this M3Y SO potential provides good predictions up to 65 MeV for $\sigma(\theta)$ and $A_y(\theta)$, it becomes less and less reliable as the energy increases. Figure 3 highlights this degradation (see dotted curves) for protons incident on ^{58}Ni. Thus, we have considered alternate prescriptions for the SO potential, namely (i) the prescription of Scheerbaum [45,50], and (ii) that of Dover and Van Giai [51].

With the prescription of Scheerbaum, the complex spin-orbit potential for incident neutrons (protons) is defined as

$$V^{\mathrm{so}}_{n(p)}(r)=\lambda_{v_{\mathrm{so}}}U^{\mathrm{so}}_{n(p)}(r), \tag{28}$$

$$W^{\mathrm{so}}_{n(p)}(r)=\lambda_{w_{\mathrm{so}}}U^{\mathrm{so}}_{n(p)}(r), \tag{29}$$

with the form factor

$$U^{\mathrm{so}}_{n(p)}(r)=\frac{1}{r}\frac{d}{dr}\left(\frac{2}{3}\rho_{p(n)}+\frac{1}{3}\rho_{n(p)}\right), \tag{30}$$

where $\rho_{n(p)}$ is the neutron (proton) radial density, and $\lambda_{v_{\mathrm{so}}}$ and $\lambda_{w_{\mathrm{so}}}$ are the real and imaginary SO potential depth normalizations, respectively. As a consequence of Eq. (30), the neutron and proton SO interactions will display radial shape differences larger than those for the proton and neutron distributions discussed below (in Sec. III C).

The SO potential form factor inspired from Dover and Van Giai's work is

$$U_{\mathrm{so}}=[1+\alpha\rho(r)]^{-1}\frac{1}{r}\frac{d\rho}{dr}, \tag{31}$$

TABLE II. Present coefficients f_{ij} in the expression (15).

$i\backslash j$	1	2	3	4
1	$+0.4596\times10^{+3}$	$-0.6440\times10^{+1}$	$+0.4040\times10^{-1}$	-0.9009×10^{-4}
2	$-0.7693\times10^{+4}$	$+0.1464\times10^{+3}$	$-0.1025\times10^{+1}$	$+0.2337\times10^{-2}$
3	$+0.5525\times10^{+5}$	$-0.1112\times10^{+4}$	$+0.7967\times10^{+1}$	-0.1802×10^{-1}
4	$-0.1437\times10^{+6}$	$+0.3038\times10^{+4}$	$-0.2220\times10^{+2}$	$+0.5026\times10^{-1}$

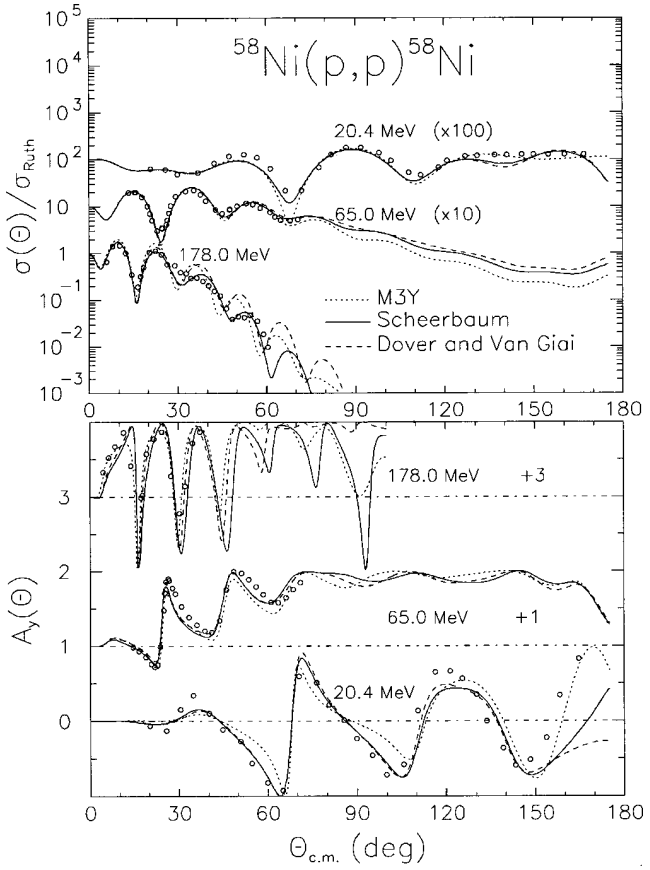

FIG. 3. Comparison between $\sigma(\theta)/\sigma_{\mathrm{Ruth}}$ and $A_y(\theta)$ predictions using three different prescriptions for the spin-orbit potential and experimental results for the $^{58}\mathrm{Ni}(\vec{p},p)^{58}\mathrm{Ni}$ reaction at 20.4, 65, and 180 MeV. Solid lines denote usage of the Scheerbaum prescription, dotted lines denote usage of the M3Y prescription, and dashed lines denote usage of the Dover and Van Giai prescriptions. Note that the differential cross sections at 65(180) MeV are offset by a factor of $10^2(10^4)$, and the analyzing powers are offset by 1(3). The LDA (27) is used for this calculation. The experimental values are shown as open circles.

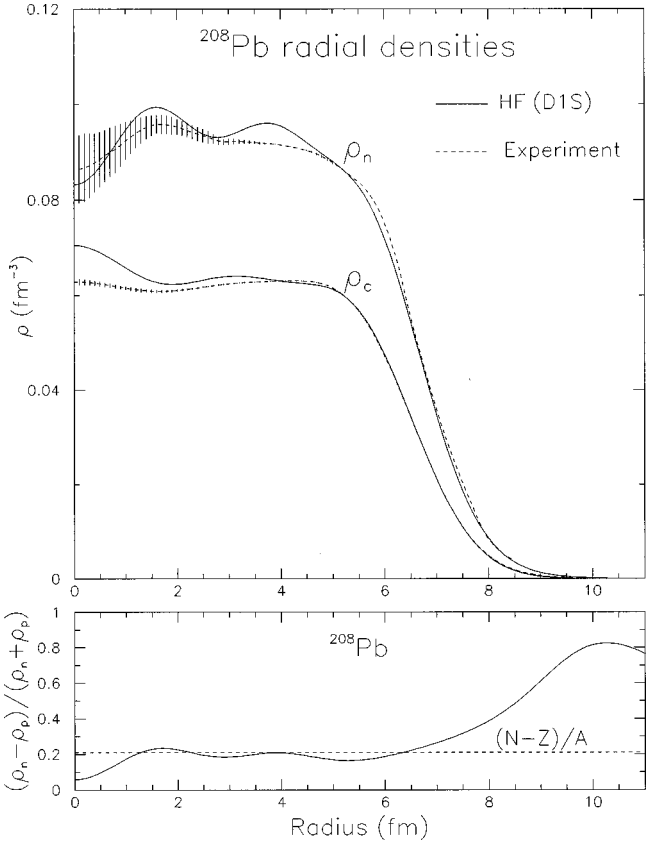

FIG. 4. Upper panel: charge and neutron radial densities for ^{208}Pb. Comparison between the present HFB predictions (continuous curves) and experimental results (hashed area and dashed curves). Lower panel: calculated $(\rho_n-\rho_p)/(\rho_n+\rho_p)$ ratio (solid line) compared with the $(N-Z)/A$ ratio (dashed line) for ^{208}Pb.

with $\alpha=4.89$ fm^3 and $\rho=\rho_n+\rho_p$. This SO radial shape does not induce difference between proton and neutron SO potentials, but the peak value of U_{so} at the surface is shifted towards large r values by the $[1+\alpha\rho(r)]^{-1}$ factor yielding a slightly larger rms radius. In Eqs. (28) and (29), we have assumed that $\lambda_{v_{\mathrm{so}}}$ and $\lambda_{w_{\mathrm{so}}}$ do not depend on the isospin of the probe. We did this because their respective empirical values deduced from our scattering analyses (see Sec. V) are identical within uncertainties.

C. Nucleon densities

In many previous OMP studies based on the JLM model, the nucleon densities have been derived from electron scattering measurements; the pointlike proton density is extracted from the measured charge density of the nucleus by deconvoluting the proton charge smearing, and the neutron density is often obtained through scaling the proton density by a N/Z factor. For this way of getting the neutron density to be justified, the assumption of a constant scaling factor between proton and neutron densities must be valid, which is nearly the case only for self-conjugate nuclei. However, microscopic calculations of the densities using the Hartree-Fock-Bogoliubov (HFB) [52] method with the Gogny D1S [53] force (see below) show that this assumption of a constant scaling factor does not hold well. A typical set of neutron and charge radial densities calculated in this manner for ^{208}Pb is shown[1] in the upper panel of Fig. 4, and compared with experimental measurements [54,55] of the same quantities. The densities exhibit some oscillations in the nuclear interior, clearly showing that the ratio between neutron and proton densities is not constant in this region. The lower panel of Fig. 4 shows the calculated ratio $\alpha=(\rho_n-\rho_p)/(\rho_n+\rho_p)$ for ^{208}Pb, to be compared with $(N-Z)/A$. As can be seen, α differs from $(N-Z)/A$ by as much as 80% at small distance, a region of minor importance for predicted scattering patterns. In contrast, the difference is typically of the order of 10% at the nuclear surface which is the region that is mostly probed by the incoming particle. If ignored, this difference could lead to an erroneous evaluation of the isovector parts V_1 and W_1 of the complex OMP.

The advantage of using microscopic densities is that it is possible to calculate OMPs for nuclei whose densities have

[1] ^{208}Pb is a doubly closed-shell nucleus, in which no pairing is present. For this reason, the Hartree-Fock-Bogoliubov and the Hartree-Fock solutions coincide.

TABLE III. $\sigma(\theta)$ and $A_y(\theta)$ database for neutron elastic scattering.

Target	Reference	Energy	Reference	Energy
^{40}Ca	[58]	2.1, 3.3, 5.3, 5.9, 6.5, 7.9 MeV	[62]	11, 20, 26 MeV
	[59]	9.9, 11.9, 13.9 MeV	[63]	19 MeV
	[60]	11 MeV	[64]	21.6 MeV
	[61]	19.6 MeV	[65]	30.3, 40 MeV
^{56}Fe	[67]	4.6, 5, 6.1, 6.5, 7.6 MeV	[11]	14.7 MeV
	[68]	5 MeV	[64]	21.6 MeV
	[69]	8, 10, 12, 14 MeV	[70]	24.8 MeV
	[8]	11, 20, 26 MeV		
^{54}Fe	[71]	8, 10, 12, 14 MeV	[72]	10, 14, 17 MeV
^{nat}Fe	[73]	24 MeV	[74]	65 MeV
^{58}Ni	[80]	8, 10, 12, 14 MeV	[81]	24 MeV
	[72]	10, 14, 17 MeV		
^{60}Ni	[80]	8, 10, 12, 14 MeV	[81]	24 MeV
^{63}Cu	[82]	5.5, 7, 8.5 MeV	[69]	8, 9.9, 11.9, 13.9 MeV
^{nat}Cu	[83]	84 MeV	[85]	136 MeV
	[84]	96 MeV	[86]	155 MeV
^{65}Cu	[82]	5.5, 7, 8.5 MeV	[87]	10, 14 MeV
	[71]	8, 10, 12, 14 MeV		
^{90}Zr	[88]	1.5 MeV	[91]	5.9, 6.9, 7.8 MeV
	[89]	1.8, 2, 3, 4 MeV	[92]	8, 10, 24 MeV
	[90]	2.2, 5.2 MeV	[93]	11 MeV
^{93}Nb	[46]	7, 8, 11 MeV	[94]	10, 12, 14, 14.6, 17 MeV
^{120}Sn	[95,96]	1, 1.6, 4 MeV	[98]	10, 11, 14, 17 MeV
	[97]	2 and 3 MeV		
^{116}Sn	[98]	10, 11, 14, 17 MeV	[99]	24 MeV
^{nat}Sn	[73]	24 MeV	[74]	65 MeV
^{208}Pb	[101]	2 MeV	[105]	30.3, 40
	[9]	4, 5, 6, 7 MeV	[74]	65 MeV
	[102]	6, 7, 8, 9, 10, 14, 17 MeV	[83]	84 MeV
	[103]	9, 11, 20, 25.7 MeV	[84]	96 MeV
	[104]	22, 24 MeV	[85]	136 MeV
	[73]	24 MeV	[86]	155 MeV
^{209}Bi	[107]	2, 2.5, 3, 3.5, 4, 4.5, 6, 6.5, 7, 7.5, 8, 9, 10, 11, 12, 20, 21.6, 24 MeV	[108]	14.6 MeV
			[73]	24 MeV
	[9]	5 MeV		

never been measured or can hardly be measured, for instance in the case of isomeric targets. For the reasons above, we have systematically adopted the nucleon densities calculated in the HFB framework for our OMP analyses. Moreover, since HFB calculations have been shown to successfully reproduce the experimental nuclear charge [52,56,57] and matter distributions as in Fig. 4, using HFB nuclear densities sets our OMP calculations on solid ground.

IV. OMP ANALYSES

A. Experimental database

In this section we detail the content of the experimental database which we have used in this study. The reader who is not interested in the origin of the data used in this study can directly jump to Sec. IV B. Tables III and IV hold the references for the $\vec{n}+X$ and $\vec{p}+X$ experimental angular distribu-

TABLE IV. $\sigma(\theta)$ and $A_y(\theta)$ database for proton elastic scattering.

Target	Reference	Energy	Reference	Energy
^{40}Ca	[109]	14.5, 18.6, 19.6, 21 MeV	[117]	61.4 MeV
	[110]	16 MeV	[111]	65 MeV
	[112]	21, 48, 49 MeV	[118]	75, 152 MeV
	[113]	26.3, 30.3 MeV	[119]	80.2, 160, 181 MeV
	[114]	30.3 MeV	[120]	135.1 MeV
	[115]	35.5, 45.5 MeV	[121]	156 MeV
	[116]	40 MeV	[26,122]	200 MeV
^{56}Fe	[125]	11, 11.7 MeV	[130]	19.1 MeV
	[126]	14.5 MeV	[114]	30.3 MeV
	[127]	15.3, 17.2, 20.4, 24.6 MeV	[131]	40 MeV
	[110]	16 MeV	[132]	49.4 MeV
	[128]	17.8 MeV	[111]	65 MeV
	[129]	18.6 MeV	[121]	156 MeV
^{54}Fe	[133]	9.8 MeV	[134]	12 MeV
	[126]	10.5, 14.5 MeV		
^{nat}Fe	[135]	155 MeV	[137]	182 MeV
	[136]	179 MeV		
^{58}Ni	[126]	10 MeV	[140]	22 MeV
	[138]	10.7, 14.5, 15.4 MeV	[113,114]	30.3 MeV
	[125]	12 MeV	[141]	35 MeV
	[110]	16 MeV	[116]	40 MeV
	[128]	17.8 MeV	[117]	61.4 MeV
	[129]	18.6 MeV	[111]	65 MeV
	[127]	20.4, 24.6 MeV	[142]	178 MeV
	[139]	21.3 MeV	[143]	200 MeV
^{nat}Ni	[144]	10 MeV	[147]	38 MeV
	[145]	12 MeV	[135]	155 MeV
	[146]	17.3 MeV		
^{60}Ni	[126]	10, 14.5 MeV	[127]	20.4, 24.6 MeV
	[138]	10.7, 14.5 and 15.4 MeV	[114,113]	30.3 MeV
	[110]	16 MeV	[111]	65 MeV
	[129]	18.6 and 19.1 MeV		
^{90}Zr	[133]	9.8 MeV	[132]	49.4 MeV
	[110]	16 MeV	[117]	61.4 MeV
	[148]	18.8 MeV	[111]	65 MeV
	[149]	22.5 MeV	[120,119]	79.6, 79.8, 98.7, 134.8, 135.1, 160, 180 MeV
	[150]	20.3 MeV	[152]	100.4 MeV
	[151]	30 MeV	[121]	156 MeV
	[116]	40 MeV		
^{120}Sn	[133]	10 MeV	[155]	40 MeV
	[110]	16 MeV	[152]	100.4 MeV
	[153]	20.4, 24.6 MeV	[119]	104 MeV
	[154]	30 MeV	[121]	156 MeV
	[114]	30.3 MeV	[156]	160 MeV
^{116}Sn	[126]	10, 14.5 MeV	[158]	20.4 MeV
	[110]	16 MeV	[132]	49.4 MeV
	[109]	18.6, 20.8 MeV	[117]	61.4 MeV
^{208}Pb	[159]	11, 12, and 13 MeV	[117]	61.4 MeV
	[110]	16 MeV	[111]	65 MeV
	[160]	21, 24.1, 35, 45, 47.3, 155, 185 MeV	[120]	79.9, 100.4, 121.2, 182.4 MeV
	[113]	26.3 MeV	[119]	79.9, 98, 185 MeV
	[114,161]	30.3	[121]	156 MeV
	[116]	40 MeV	[156]	160 MeV
	[132]	49.4 MeV	[162–164]	201 MeV
^{209}Bi	[110]	16 MeV	[118]	78, 153 MeV
	[165]	57 MeV	[121]	155 MeV
	[111]	65 MeV		

tions used in this study. Note that no data for $Q(\theta)$ and $R(\theta)$ spin rotation functions is included in this database, so that the calculated $Q(\theta)$ and $R(\theta)$ values presented in Sec. VI B are plain predictions. The neutron total cross sections are from [33,66] for ^{40}Ca, [75–79] for ^{nat}Fe, [75,76,79] for ^{nat}Ni, [33,75] for ^{nat}Cu, [33,89] for ^{90}Zr, [33,100] for ^{nat}Sn, and [33,75,106] for ^{208}Pb. The proton reaction cross sections come from [123,124] for ^{40}Ca, [123,124] for ^{56}Fe, [123,124,141] for ^{58}Ni, [123] for ^{63}Cu, [123] for ^{90}Zr, [123,157] for ^{120}Sn, and from [123,124] for ^{208}Pb.

B. Codes

Two codes are used for the calculation of scattering and reaction observables. The first one FLIT [166] generates folding potentials on a radial mesh. This code has been slightly modified to include the new JLM parameters gathered in Tables I and II, as well as the new expressions (21),(22) for ϵ_F. The numerical files generated for the central and spin-orbit potentials are used as input for ECIS95 [167]. This versatile code includes provisions for treating the compound scattering process [168,169] as well as the Mott-Schwinger interaction [170–172] which plays an important role in the interpretation of analyzing powers for neutrons scattered at forward angles.

Finally, the semimicroscopic OMP used in the present work has the form

$$\begin{aligned} U(r,E) = {} & \lambda_v [V_0(r,E) + \alpha(r) V_1(r,E)] \\ & + i\lambda_w [W_0(r,E) + \alpha(r) W_1(r,E)] \\ & + \frac{\hbar^2}{2m^2c^2} \vec{\ell} \cdot \vec{\sigma} [\lambda_{v_{so}} V_{so}(r) + i\lambda_{w_{so}} W_{so}(r)] \\ & + \frac{\hbar^2}{2m^2c^2} \mu \vec{\ell} \cdot \vec{\sigma} \frac{1}{r} \frac{d}{dr} V_c(r) \end{aligned} \tag{32}$$

for incident neutrons. In Eq. (32) (i) the λ_i's are E-dependent normalization coefficients, (ii) μ is the neutron magnetic moment, (iii) V_{so} and W_{so} are the spin-orbit form factors (28),(29), and (iv) V_0, V_1, W_0, and W_1 are the isoscalar and isovector components of the central potential calculated from nuclear matter through an improved LDA to be chosen later on in Sec. IV D. $V_c(r)$ is the Coulomb potential which also contributes to the proton potential. The proton-nucleus OMP adopted here includes $V_c(r)$ and has the form (32) from which the last component (i.e., the Mott-Schwinger interaction) is removed since its effect on the predictions is negligible. In the present calculations, the complex potential seen by an incident proton with energy E is evaluated at $E - V_c$. Whether this prescription is valid or not for the imaginary central component will be discussed below. Relativistic kinematics [160] is used throughout this study. Finally, for odd target nuclei, the contribution stemming from the spin-spin interaction as well as other small components of the residual nucleon-nucleus potential [19] was ignored in the present study. The effects of the spin-spin interaction are indeed very weak as shown in Fig. 4 of [173] in which the experimental angular distributions measured for 9 MeV neutrons incident on ^{208}Pb ($I=0$) and ^{209}Bi ($I=9/2$) coincide nearly perfectly.

C. Grid searches

Here we explain the method adopted to optimize the values of the model parameters as well as the prescriptions (for the LDA and the SO potential) adopted in actual OMP calculations based on the JLM model.

In the first step, we have considered the proton database because it includes many $\sigma(\theta)$ and $A_y(\theta)$ measurements up to 200 MeV. Wherever possible, we used the ranges of values of λ_v, λ_w, $\lambda_{v_{so}}$, $\lambda_{w_{so}}$, t_r, and t_i available from previous works as coarse starting values for our search. For each target nucleus considered separately, we performed single shot best fit OMP calculations at each incident energy whenever $\sigma(\theta)$ and/or $A_y(\theta)$ data is available. Note that one does not have a strong constraint on the SO components unless an analyzing power measurement is available. Similarly, it is difficult to precisely determine the central OMP component without differential cross section distribution. At this point, it is important to focus on getting a fit quality that is as constant as possible, and identify the peculiarities of individual datasets so that one does not attempt to match a clearly erroneous feature of an angular distribution. Thus we have excluded a few lower quality datasets from our database. Also, for incident protons, we have allowed the experimental normalization of some $\sigma(\theta)$ distributions (often extracted from printed figures) to vary by as much as 10% when such a change significantly improves the quality of our fit.

Once this exercise has been completed for many nuclei, the various parameters entering the OMP are put together and plotted (see Figs. 5 and 6). Clear cut patterns begin to show up, which are given smooth close forms. These close forms are then inserted as inputs to new OMP calculations. The parameters governing our close forms are tuned until (i) the best fit λ's display the lowest possible dispersion around the E-dependent close form, and (ii) the visual inspection of individual angular distributions does not reveal any systematic bias as a function of energy. One must then check that the current close forms do not spoil fits in any portion of the mass range explored, and constitute a good compromise with constant quality fits over the full $40 \leqslant A \leqslant 209$ range for tested nuclei. This tedious exercise eventually gets to an end when all the various LDA and SO prescriptions have been tested.

In the second step, the above techniques have been used for incident neutrons, the only difference being that we allowed a few normalizations for the experimental $\sigma(\theta)$ distributions to vary by as much as 5% (instead of 10% for incident protons).

The last stage in these analyses has been the fine tuning of the range parameters t_r and t_i which weakly influence the predicted angular distributions but have a noticeable effect on the overall magnitude of reaction cross sections. The finally adopted range parameters are trade-off values, fixed in such a way that all the proton reaction and neutron total cross sections are equally well described across the mass and energy ranges sampled in the present study.

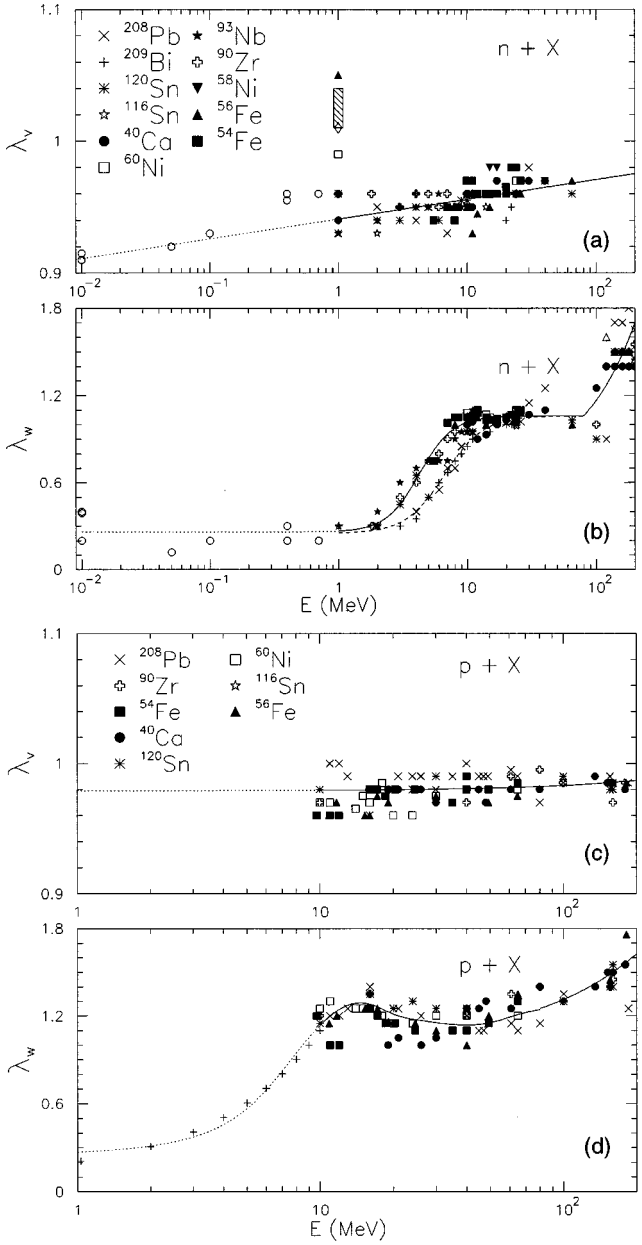

FIG. 5. Normalization factors for the central part of the OMP for neutrons [(a) and (b)], and for protons [(c) and (d)]. Panel (a) shows the normalizations of the real part of the neutron OMP and panel (b) shows the normalizations of the imaginary part of the neutron OMP. Panels (c) and (d) show, respectively, the normalization of the real and imaginary parts of the proton OMP. The open circles represent the values that give the best fits to the average resonance parameters S_0 and R', and the other symbols represent the values that produce the best fits to the differential cross section and analyzing power distributions. At 1 MeV, the symbols represent the values that give acceptable fits to the measured total cross sections. The hatched box encloses the best fits parameters for ^{75}As, ^{80}Se, ^{103}Rh, and ^{109}Ag. The solid lines represent the variations of the normalization factors with energy. Whenever these parametrizations are not thoroughly tested, dotted lines are used.

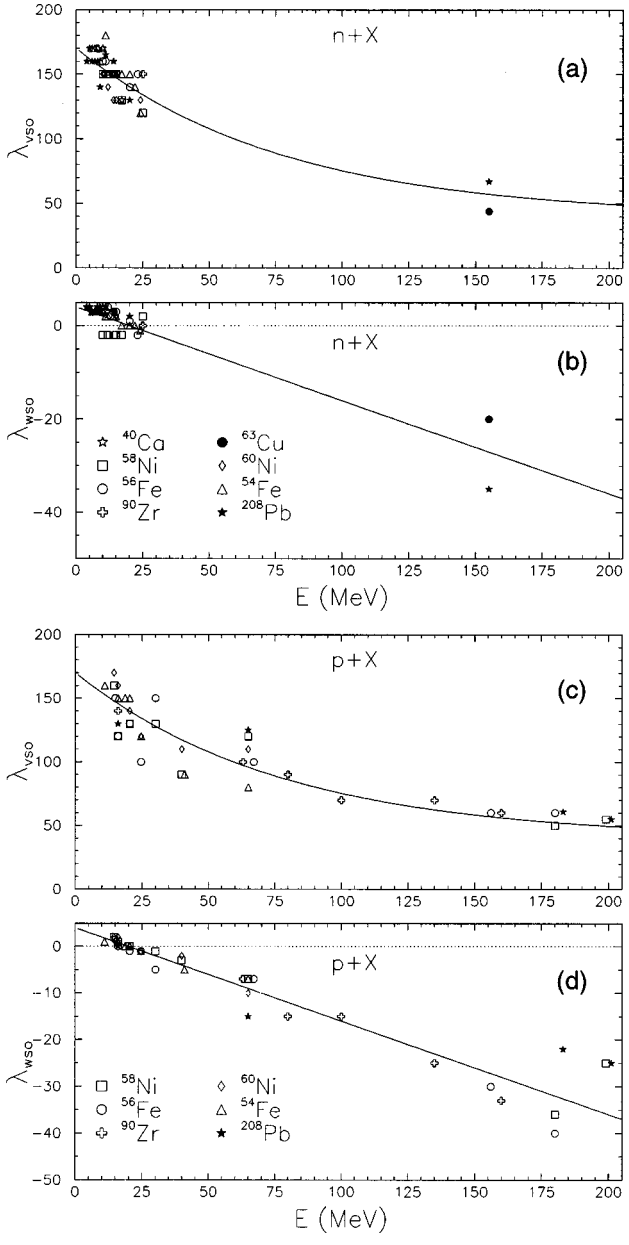

FIG. 6. Normalization factors for the spin-orbit potential: (a) and (b) for protons, and (c) and (d) for neutrons. (a) and (c) are for the real SO potential while (b) and (d) are for the imaginary SO potential. The symbols represent the values of the normalization factors that produce best fits to the differential scattering cross section and analyzing power data.

D. Selected LDA prescription

We have tested the three options (see Sec. III A) for the position at which the interaction is evaluated, in the 1 to 200 MeV energy range, and for $40 \leqslant A \leqslant 209$ nuclei. While at low energies all three prescriptions can, to some extent, reproduce the experimental data given adequate potential depth normalizations, at energies in excess of 100 MeV the interaction evaluated at the target position (27) gives the most satisfying fit of the three prescriptions. Figure 7 shows a comparison of differential cross sections, analyzing powers, and spin rotation functions calculated with the three above prescriptions for the reaction $^{208}\mathrm{Pb}(\vec{p},p)^{208}\mathrm{Pb}$ at 201 MeV. The calculations shown were performed with our final potential, using the potential depth normalizations that give the best fit for the interaction evaluated at the target position. However, even with tuned normalizations, the interaction evaluated at the projectile position completely fails to repro-

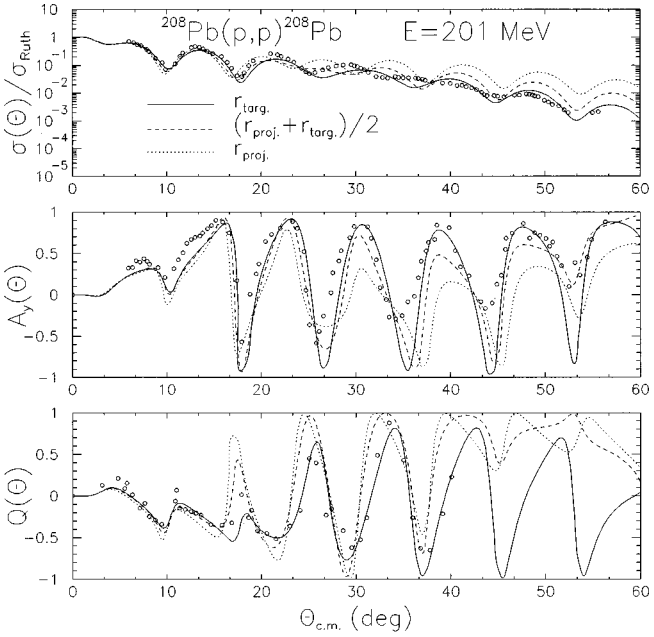

FIG. 7. Calculated $\sigma(\theta)/\sigma_{\mathrm{Ruth}}$ (upper panel), $A_y(\theta)$ (middle panel), and $Q(\theta)$ (lower panel) distributions for the reaction $^{208}\mathrm{Pb}(\vec{p},p)^{208}\mathrm{Pb}$ at 201 MeV. The evaluation of the effective interaction is performed at r_{proj} [LDA prescription (25), dotted line], $(r_{\mathrm{proj}}+r_{\mathrm{targ}})/2$ [LDA prescription (26), dashed line] and r_{targ} [LDA prescription (27), solid line]. The experimental values are shown as open circles.

duce the data at high energy. On the other hand, with appropriate normalizations, the interaction evaluated at the midpoint produces fits that are slightly worse than those of the interaction evaluated at the target position. From this point on, we will use the prescription which evaluates the effective interaction at the target position (27), since this prescription leads to best overall agreement with experimental data.

E. Selected SO potential prescription

The three SO prescriptions introduced in Sec. III B have been tested through systematic comparisons between OMP predictions and differential scattering cross section and analyzing power measurements. This is illustrated in Fig. 3 for polarized protons incident on ^{58}Ni at 20, 65, and 178 MeV. Except for the highest incident energy where the Scheerbaum prescription clearly provides the best overall description of the data, these SO prescriptions produce fits of comparable quality. Since similar features are observed throughout our systematic investigation, we use the SO potential of Eqs. (28)–(30) for the rest of this study.

V. OPTIMAL PARAMETERS

The normalization factors (λ_v,λ_w) and $(\lambda_{v\mathrm{so}},\lambda_{w_{\mathrm{so}}})$ obtained for the complex central and spin-orbit potentials, respectively, are discussed separately for incident protons and neutrons. The discussion relevant to the range parameters t_r and t_i is also included in this section.

A. Normalization for the neutron central OMP

The normalization factors λ_v and λ_w obtained between 1 and 200 MeV from individual best fits to elastic scattering (below 100 MeV) and total (above 100 MeV) cross-section measurements forming our database (see Sec. IV A) are shown in Fig. 5. This figure also includes the λ's from best fit to s-wave strength functions (S_0) and potential scattering radii (R') determined below 1 MeV (open circles) [174]. Various symbols are used to mark the λ's corresponding to specific target nuclei. The λ_v's and λ_w's form clearcut patterns that can be parametrized as functions of energy all the way to 200 MeV.

1. λ_w values

In Fig. 5(b), the best fit values of λ_w exhibit strong energy dependences in the 1–10 MeV and 100–200 MeV ranges, and remain nearly constant ($\lambda_w \approx 1.06$) between 10 and 100 MeV. Another plateau ($\lambda_w \approx 0.25$) is present between 1 keV and 1 MeV. The fact that the normalization factor is significantly different from unity below 10 MeV suggests that the JLM model is not accounting for specific structure effects and/or that the absorption at low energy reflects the importance of compound processes which are outside the scope of the JLM model. On the other hand, the sharp increase observed at high energies may be related to the opening of pion channels [33,175] that are not treated in the JLM model.

A closer look at the pattern formed by the λ_w's in Fig. 5(b) suggests a splitting of their values into two families for $E \leqslant 10$ MeV. One family consists in ^{40}Ca, ^{208}Pb, and ^{209}Bi, the other one includes all the other nuclei of our sample. We have parametrized our results below 80 MeV as

$$\lambda_{w_{\mathrm{DM}}}(E) = 1.06 - 0.81\left[1+\exp\left(\frac{\ln(1000E)-8.80}{0.35}\right)\right]^{-1} \tag{33}$$

and

$$\lambda_{w_{\mathrm{NDM}}}(E) = 1.06 - 0.80\left[1+\exp\left(\frac{\ln(1000E)-8.35}{0.30}\right)\right]^{-1}, \tag{34}$$

where E is the incident neutron energy in MeV. $\lambda_{w_{\mathrm{DM}}}(E)$ is the imaginary potential depth normalization for doubly magic nuclei (^{40}Ca, ^{208}Pb, and ^{209}Bi which is close to being doubly magic), and $\lambda_{w_{\mathrm{NDM}}}(E)$ for the non-doubly-magic nuclei. Below 10 MeV we find that $\lambda_{w_{\mathrm{DM}}} < \lambda_{w_{\mathrm{NDM}}}$; this is a measure of the well known shell effects on the absorptive potential. At low incident energy, the absorption is weaker for doubly magic nuclei. Above 10 MeV, this structure effect vanishes.

The strong increase of λ_w observed for $E > 80$ MeV is essential in order to get good fits to the total cross sections. In this energy domain, we have thus introduced a multiplicative factor $f_\pi(E)$ that applies to the expressions (33) and (34)

$$f_\pi(E) = 1 + 5\times 10^{-3}(E-80) \quad (E \geqslant 80 \text{ MeV}). \tag{35}$$

2. λ_v values for $E > 6$ MeV

The best fit λ_v values are shown as various symbols in

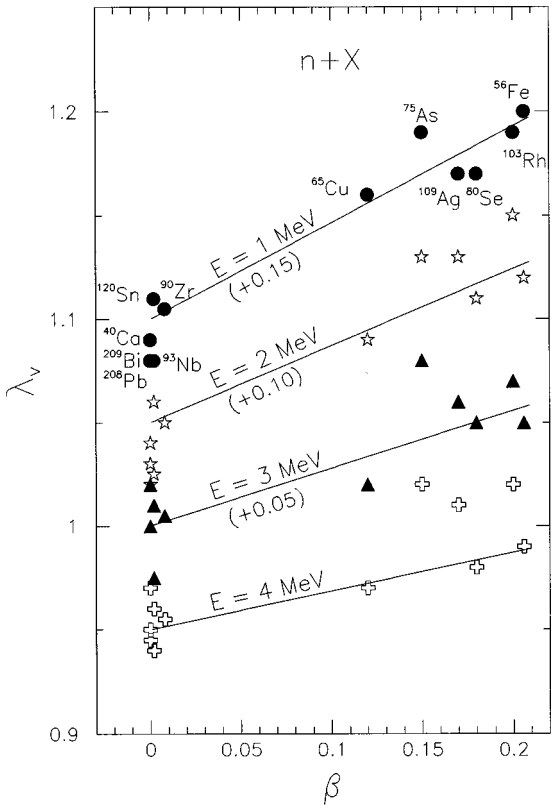

FIG. 8. Evolution of λ_v(neutron) in the 1 to 4 MeV range, as a function of the target deformation parameter β. The lines represent our parametrization (37) and (38).

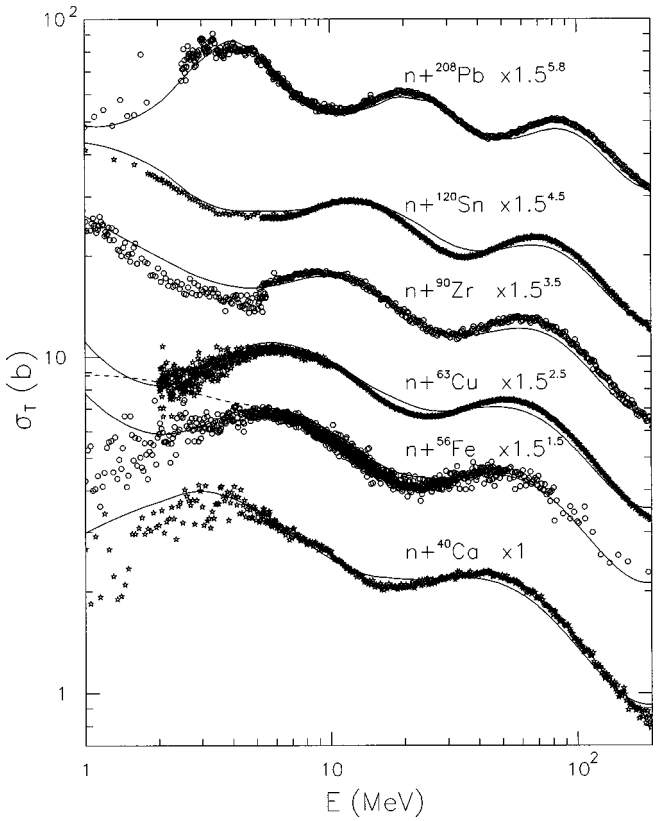

FIG. 9. Comparison between calculated and experimental total cross sections for neutrons incident on ^{40}Ca, ^{56}Fe, ^{63}Cu, ^{90}Zr, ^{120}Sn, and ^{208}Pb. The solid lines represent the results of the calculations using our global OMP and the dashed line shows the result of our calculation without the low energy deformation correction in (37) for ^{56}Fe.

Fig. 5(a). Those included in a box[2] as well as the other normalizations shown at 1 MeV will be discussed below. For the time being, we restrict the discussion to the normalization factors fixed at $E>6$ MeV. In Fig. 5(a), the λ_v's display a near constant behavior around $\lambda_v \approx 0.95$. However, the normalization factors follow a slightly increasing trend with energy which is given the form

$$\lambda_{v_{\mathrm{BG}}}(E) = 0.0065 \ln(1000E) + 0.896. \tag{36}$$

We label Eq. (36) as the background normalization factor for the neutron central potential.

3. λ_v values for $1 \leqslant E \leqslant 6$ MeV

In the $1 \leqslant E \leqslant 6$ MeV energy range, the total cross section predictions are very sensitive to minute variations of the real potential depth and therefore to λ_v. The λ_v values have thus been fine-tuned to produce acceptable fits to the total cross sections without spoiling the fits to the differential scattering measurements. The results are shown in Fig. 8 at 1, 2, 3, and 4 MeV for several nuclei, and displayed as functions of the quadrupole deformation β obtained from our HFB calculations. Note that all the nuclei shown in Fig. 8 have positive β values. The highest deformation, $\beta = 0.22$, is found for ^{56}Fe which is a slightly deformed nucleus as suggested by its level sequence at low spin and excitation energy [176].

[2]These parameters are for ^{75}As, ^{80}Ce, ^{103}Rh, and ^{109}Ag target nuclei which have barely been considered in this work.

At $E=1$ MeV, the λ_v's are ranging from 0.93 to 1.03. This interval of values gets narrower as the energy increases. Since the λ_v's values are determined to less than 2%, all these results are meaningful and do not reflect either bias or ambiguities in our OMP analyses. As a consequence, there is a clear correlation between the normalization λ_v and the deformation β. More precisely, λ_v increases with β, and this trend gets stronger as E decreases down to 1 MeV. These features are the signature of nuclear structure effects in the real central potential which show the limits of using a spherical optical model for slightly deformed nuclei.

To cure this problem without resorting to coupled channels calculations, the normalization factor for the real central potential has been given the functional form $\lambda_v(E,\beta)$ in the interval $1 \leqslant E \leqslant 6$ MeV for positive values of the deformation β. $\lambda_v(E,\beta)$ connects smoothly with the background form (36)

$$\lambda_v(E,\beta) = f_l(E,\beta)\lambda_{v_{\mathrm{BG}}}(E), \tag{37}$$

with

$$f_l(E,\beta) = 1 + (0.00379 + 0.0979\beta)(6 - E). \tag{38}$$

This parametrization is shown as a set of continuous lines in Fig. 8 where it can be seen to roughly account for the

empirical λ_v values fitted for $1 \leqslant E \leqslant 6$ MeV. We have thus established a continuous form for the λ_v normalization factor between 1 and 200 MeV.

The impact of using Eqs. (36) and (37) on the σ_T predictions is illustrated for ^{56}Fe in Fig. 9. The dashed and continuous curves represent the present JLM calculations using $\lambda_{v_{\rm BG}}(E)$ and $\lambda_v(E,\beta)$, respectively. It is clear that a spectacular improvement in the σ_T prediction is obtained using Eq. (37).

B. Normalization for the proton central OMP

The normalization factors λ_v and λ_w optimized for incident protons using grid search techniques (Sec. IV C) are now discussed.

1. λ_w values

The parameter λ_w takes on values which depend on whether the imaginary potential is evaluated at E or $E - V_c$. While in the original JLM model references [37,43] the complex central potential was to be evaluated at $E - V_c$, it has been argued more recently [177] that the imaginary OMP component should be evaluated at E instead of $E - V_c$. Since it is not entirely clear to us at which energy the absorption should be evaluated, we have examined both recommendations.

We start with the case for which the imaginary OMP is evaluated at $E - V_c$. The optimum normalizations factors λ_v and λ_w, labeled with various symbols, are shown in Figs. 5(c) and 5(d). Above approximately 10 MeV, the λ_i's are mainly obtained from fits to $\sigma(\theta)/\sigma_{\rm Ruth}$ and $A_y(\theta)$ data. Between 2 and 8 MeV, the λ_w values (cross symbols) are deduced by forcing the volume integral of the imaginary JLM potential for ^{90}Zr to match that deduced from a dispersive optical model analysis [178]. Focusing on the incident energies at or above the Coulomb barrier, the λ_w's range from 1.05 to 1.6 with a mean value of 1.25. One obvious feature of the λ_w's pattern is the dip it exhibits between 20 and 40 MeV, where λ_w's go from 1.25 down to 1.05 at 30 MeV. We have also observed this nearly 20% drop of λ_w's while working with the original JLM parametrization, so it is not likely that this feature was introduced by our refitting of the JLM imaginary potential. In contrast to what was observed with neutron projectiles, it is interesting to notice that there is no apparent splitting in the λ_w values for the doubly magic and the non-doubly-magic nuclei down to 10 MeV. We have fitted the E dependence of λ_w between 1 and 200 MeV

$$\lambda_w(E) = \left[1.25 - \frac{1.05}{1+\exp\left(\frac{E-6.2}{1.9}\right)} \right] \times \left[1 + 0.08 \exp - \left(\frac{E-14}{5}\right)^2 \right] \times \left[1 - 0.09 \exp - \left(\frac{E-40}{25}\right)^2 \right] \times \left[1 + \theta(E-80)\frac{E-80}{400} \right], \quad (39)$$

where E is the incident proton energy in MeV, and $\theta(x)$ is the well known step function. The last factor in Eq. (39) originates from our attempt to reproduce the reaction cross sections at high energy. This enhancement factor is very similar to the high energy factor shown in Eq. (35) for incident neutrons in the same energy range.

The comparison between previously published and present values of λ_w shows that there is good agreement for $15 \leqslant E \leqslant 40$ MeV; previously published λ_w's are of the order of 1.0 to 1.05 [8,45] while we find λ_w in the 1.0 to 1.30 range. Note the large dispersion of the present best fit normalization factors in the 20 to 50 MeV range.

We now focus on the normalization obtained when the imaginary part of the potential is evaluated at E instead of $E - V_c$. We have tried this way of evaluating the OMP, and have found that given appropriate normalizations which are not very different from those needed in the above discussion, there is not much difference between the observables calculated with one or the other prescription. Thus the quality of the fits cannot be used to decide which prescription is best. Nevertheless, for the rest of this study, we chose to use the original way of evaluating the absorption, i.e., evaluating the imaginary part of the OMP at $E - V_c$. There is, however, no compelling reason to do so, and we believe that using one or the other prescription does not affect our conclusions.

2. λ_v values

The normalization factors for the real central potential have been obtained from the analysis of $\sigma(\theta)/\sigma_{\rm Ruth}$ and $A_y(\theta)$ data available from the Coulomb barrier to 200 MeV. The individual best fit λ_v values shown in Fig. 5(d) are nearly constant between 10 and 200 MeV. Above 8 MeV, this pattern is given the close form (solid curve)

$$\lambda_v(E) = 0.979 + 0.00004E, \quad (40)$$

where E is the incident proton energy in MeV. For $E < 8$ MeV, Eq. (40) is presented as a dashed curve; this extrapolation is used later on to make plain predictions for the reaction cross section below the Coulomb barrier.

C. Spin-orbit potential depth normalization

The normalization factors of the complex SO potential, also deduced from grid search, display values which rely heavily on information conveyed by the analyzing powers. These are gathered for incident protons and neutrons in Figs. 6(a)–6(d). As can be seen, the $\lambda_{v_{\rm so}}$ values for incident protons smoothly decrease with increasing energy. Although the $\lambda_{v_{\rm so}}$'s are rather scarce for neutrons at $E > 24$ MeV, they seem to display the same pattern as that for $\lambda_{v_{\rm so}}$(proton). Similarly, the $\lambda_{w_{\rm so}}$'s for incident protons and neutrons both produce a pattern that is decreasing with energy, starting with weak positive values at low energy, becoming negative at energies in excess of 20 MeV, and finally leveling off by 180 MeV.

Typical uncertainties on $\lambda_{v_{\rm so}}$ and $\lambda_{w_{\rm so}}$ are of the order of 10% and 20%, respectively. As a result, $\lambda_{v_{\rm so}}$(proton) $\approx \lambda_{v_{\rm so}}$(neutron) and $\lambda_{w_{\rm so}}$(proton) $\approx \lambda_{w_{\rm so}}$(neutron). These

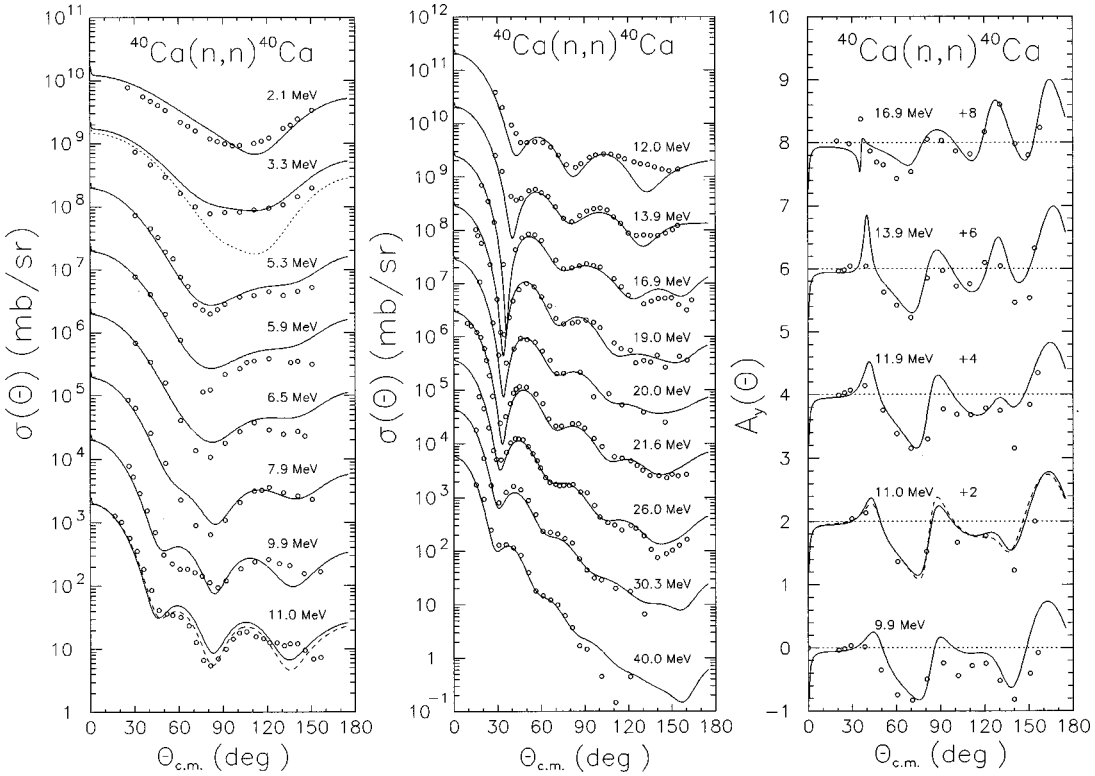

FIG. 10. Comparison of predicted differential cross sections and analyzing powers with experimental data, for neutrons scattered from ^{40}Ca between 2.1 MeV and 40 MeV. Note that the differential cross sections are offset by factors of 10, while the analyzing power distributions are shifted by 2. The solid lines represent the results of our global OMP calculations (including CN contributions), whereas dashed lines show the results of individual best fits wherever they significantly improve the description of the data. Dotted lines represent the direct interaction components of the differential cross sections.

normalization factors are then parametrized as

$$\lambda_{v_{so}} = 130 \exp(-0.013E) + 40 \tag{41}$$

and

$$\lambda_{w_{so}} = -0.2(E-20), \tag{42}$$

where E is the incident energy in MeV.

D. Ranges of the improved LDA

In order to find the values of the t_r and t_i ranges we have allowed them to vary while fitting proton reaction (σ_R) and neutron total (σ_T) cross sections for E ranging between 2 MeV (10 MeV for incident protons) and 200 MeV, and target nuclei from ^{40}Ca to ^{208}Pb. The values of the JLM range parameters that fit the cross sections over the whole range of energies and mass numbers are

$$t_r = t_i = 1.2 \ \text{(fm)} \tag{43}$$

for protons, and

$$t_r = t_i = 1.3 \ \text{(fm)} \tag{44}$$

for neutrons. Note that it is possible to get a better fit for an individual energy and/or nucleus but the values above are compromises that give a satisfying fit over the whole range of mass and energy. Also note that these values are well within the range of previously published results [8,37,45].

VI. COMPARISONS BETWEEN MEASUREMENTS AND FINAL PREDICTIONS

For calculating the following results, the final form of our global OMP's is used. The nuclear matter potential (5)–(8) is calculated using the JLM parametrizations (12)–(15) of which the imaginary component was refitted over a wider energy range. The new parameters are shown in Tables I and II as well as in Eqs. (21) and (22). We adopted the improved LDA prescription which evaluates the finite nuclei OMP at the target position (24),(27). The spin-orbit potential uses the Scheerbaum form factor (30). The nuclear radial densities used in the LDA and the SO form factors are calculated in the HFB framework using the D1S Gogny force. The frozen close forms for the central neutron (33)–(38), central proton (39),(40), and SO potential depths normalization factors (41),(42), as well as LDA range parameters (43),(44) are then applied to their respective components. This procedure yields OMPs that rest on microscopic foundations, that are free of adjustable parameters and whose unique inputs are the target proton and neutron densities, and the projectile energy and type (p or n).

Predictions for $\sigma(\theta)$, $A_y(\theta)$, $Q(\theta)$, $R(\theta)$, σ_R, and σ_T are performed and compared with experimental data available for protons and neutrons incident on selected nuclei.

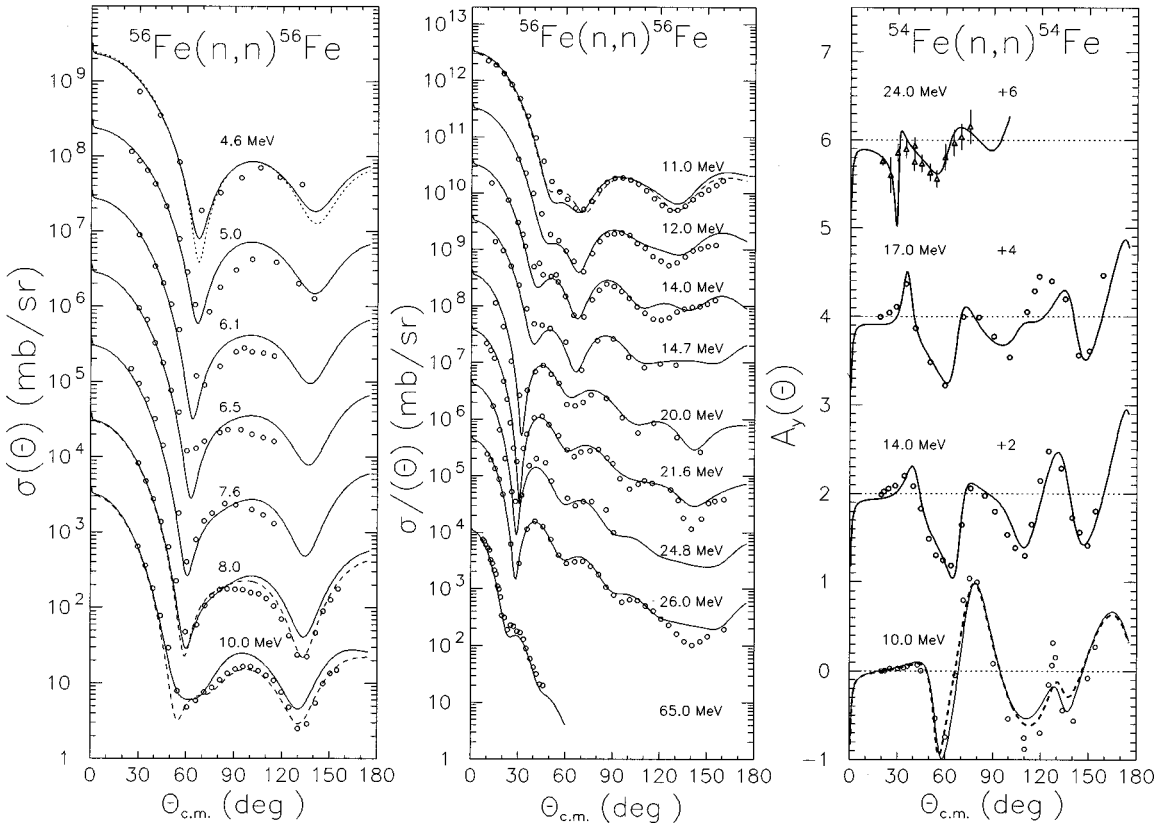

FIG. 11. Comparison of predicted differential cross sections and analyzing powers with experimental data, for neutrons scattered from ^{54}Fe, ^{56}Fe, and ^{nat}Fe between 4.6 MeV and 65 MeV. For more details, see the caption of Fig. 10.

A. $\vec{n}+X$ systems

1. ^{40}Ca target

^{40}Ca is interesting for several reasons: (i) it marks the lower end of the mass region here under study, (ii) its spherical character makes it ideal for OMP studies based on the JLM model, and (iii) it is a self-conjugate nucleus. As a by-product, the asymmetry parameter $\alpha(r)$ is close to zero and the complex isovector potential is negligible. This is an excellent opportunity to test the isoscalar OMP components alone.

Figure 10 shows comparisons between experimental $\sigma(\theta)$ and $A_y(\theta)$ data (circles) and present JLM OMP predictions ignoring (dotted curves) and including (solid curves) compound nucleus (CN) components. The CN process brings significant contributions to the $\sigma(\theta)$ and $A_y(\theta)$ predictions only below 10 MeV. The agreement between predicted and measured $\sigma(\theta)$ is quite good over the whole energy range where data is available, except near 11 MeV. However, good quality predictions are restored using best fit λ_i's parameters (dashed curves) at this incident energy. For the $A_y(\theta)$ measurements, the predictions are as satisfying as those for $\sigma(\theta)$ data. Figure 9 shows a comparison between measured (symbols) and predicted (solid curves) σ_T values from 1 to 200 MeV. The overall agreement is good, the difference between the two sets never exceeding 7%.

2. ^{54}Fe and ^{56}Fe targets

^{56}Fe is a slightly deformed nucleus. This study illustrates to which extent a spherical JLM model parametrization can be applied to the interaction of incident neutrons with moderately deformed target nuclei. Figure 11 shows that the $\sigma(\theta)$ data is well described throughout the 4.6 to 65 MeV range. Only in the vicinity of 10 MeV has the best fit (dashed curve) been found significantly better than that based on our global parametrization (solid curve). Unfortunately $A_y(\theta)$ measurements are rather scarce for this iron isotope. Thus we have relied on those available for ^{54}Fe to show that our model is again successful. The calculated $\sigma_T(^{56}\mathrm{Fe})$ cross sections (Fig. 9) match well the experimental ^{nat}Fe data which is not as precise as that for ^{40}Ca. Further discussions are postponed until the new σ_T values recently measured at Los Alamos Laboratory for the ^{54}Fe and ^{56}Fe isotopes are released.

3. ^{63}Cu target

Copper is included in our sample to test our model predictions for even-odd targets. Moreover, copper was not considered earlier while optimizing the normalization parameters (see Fig. 5). For this reason, the results shown below highlight the predictive power of our global OMP. In Fig. 12 is shown a comparison between measured and predicted differential scattering cross sections. The agreement is very good, except at 14 MeV where it could be improved using best fit λ_i parameters. At the higher energies, notwithstanding the narrow angular range covered by experimental measurements, the calculations account fairly well for the data. This good agreement at forward angles is directly related (through the optical theorem) to that obtained for the total cross sections as shown in Fig. 9. The differences occurring at angles in excess of 15° for energies greater than 80 MeV can be attributed to contamination of the experimental elastic

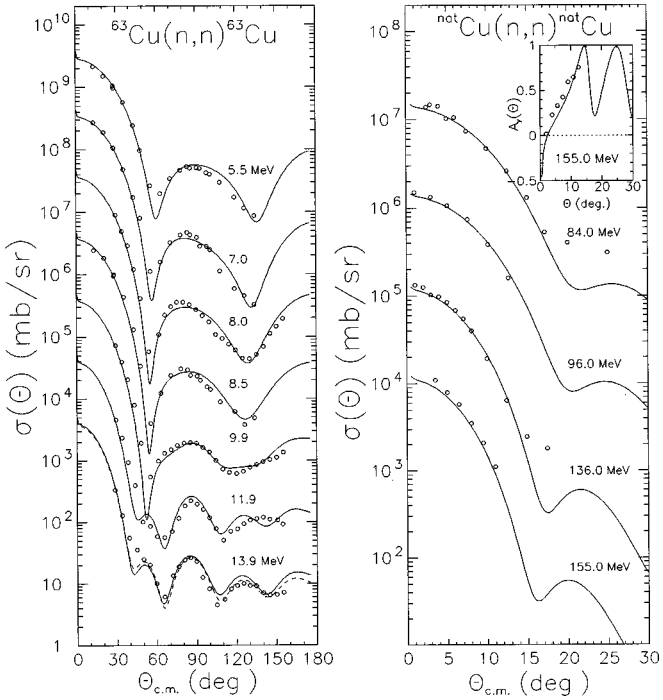

FIG. 12. Comparison of predicted differential cross sections and analyzing powers with experimental data, for neutrons scattered from ^{63}Cu and ^{nat}Cu between 5.5 MeV and 155 MeV. For more details, see the caption of Fig. 10.

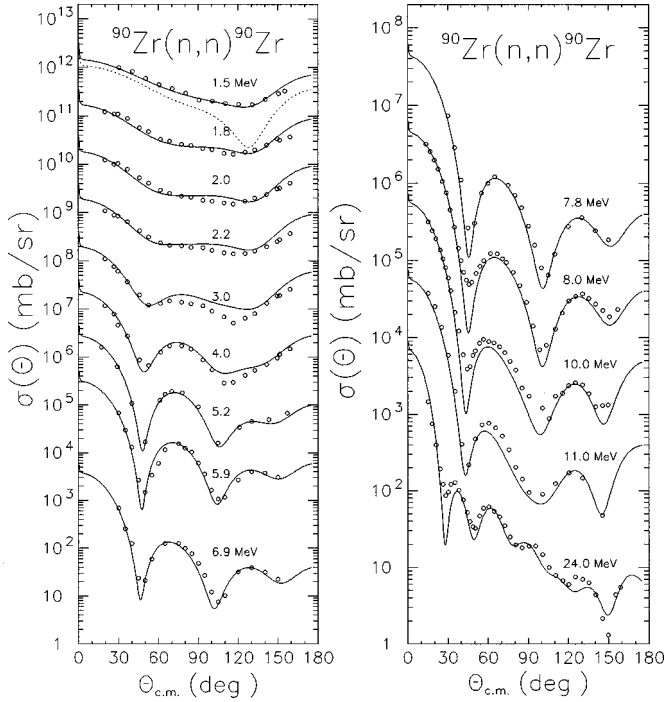

FIG. 13. Comparison of predicted differential cross sections with experimental data, for neutrons scattered from ^{90}Zr between 1.5 MeV and 24 MeV. For more details, see the caption of Fig. 10.

scattering cross sections by inelastic processes that have not been resolved in these measurements. The OMP predictions for $\sigma_T(^{nat}\mathrm{Cu})$ differ from measurements by no more than 8% over the 1 to 200 MeV energy range.

4. ^{90}Zr target

Our global semimicroscopic OMP can account for the available $\sigma(\theta)$ data with good accuracy as illustrated in Fig. 13. At lower incident energies the excellent agreement between data and predictions shows that the CN process is handled properly as well. As can be seen (Fig. 9), the OMP predictions deviate from the σ_T data by at most 10%.

5. ^{116}Sn and ^{120}Sn targets

The $\sigma(\theta)$ and $A_y(\theta)$ data available for ^{120}Sn is gathered in Fig. 14. This figure also includes $\sigma(\theta)$ data obtained at 26 and 65 MeV for ^{116}Sn and ^{nat}Sn, respectively. The OMP results are in good agreement with these experimental results and with those for the ^{nat}Sn total cross section (see Fig. 9).

6. ^{208}Pb target

^{208}Pb and ^{209}Bi are the nuclei that are the closest to nuclear matter in our sample, thus the LDA should be more reliable for heavy nuclei. If valid, these statements would explain why, for these two target nuclei, our OMP predictions reproduce almost perfectly the $\sigma(\theta)$ and $A_y(\theta)$ data. This is illustrated in Fig. 15 for ^{208}Pb. However, around 40 MeV, the prediction can further be improved by using the best fit normalizations. The total cross section $\sigma_T(^{208}\mathrm{Pb})$ is accurately predicted (Fig. 9), the data and calculations differing by at most 10% in the 6–120 MeV range.

7. ^{54}Fe, $^{58,60}Ni$, ^{93}Nb, and ^{209}Bi targets

The OMP analyses have been conducted with equal success for several other target nuclei (^{54}Fe, ^{58,60}Ni, ^{93}Nb, and ^{209}Bi). Our results for $\sigma(\theta)$, $A_y(\theta)$, and σ_T are available on request from the authors.

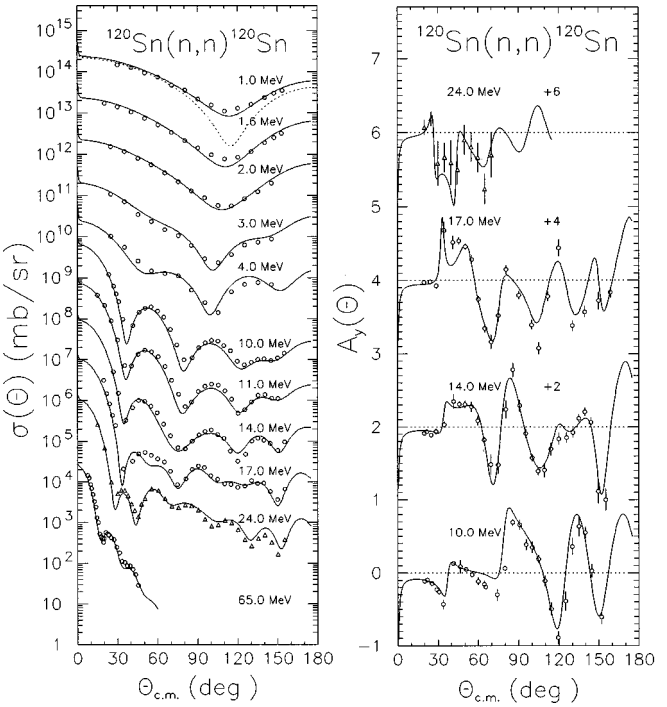

FIG. 14. Comparison of predicted differential cross sections and analyzing powers with experimental data, for neutrons scattered from ^{116}Sn, ^{120}Sn, and ^{nat}Sn between 1 MeV and 65 MeV. For more details, see the caption of Fig. 10.

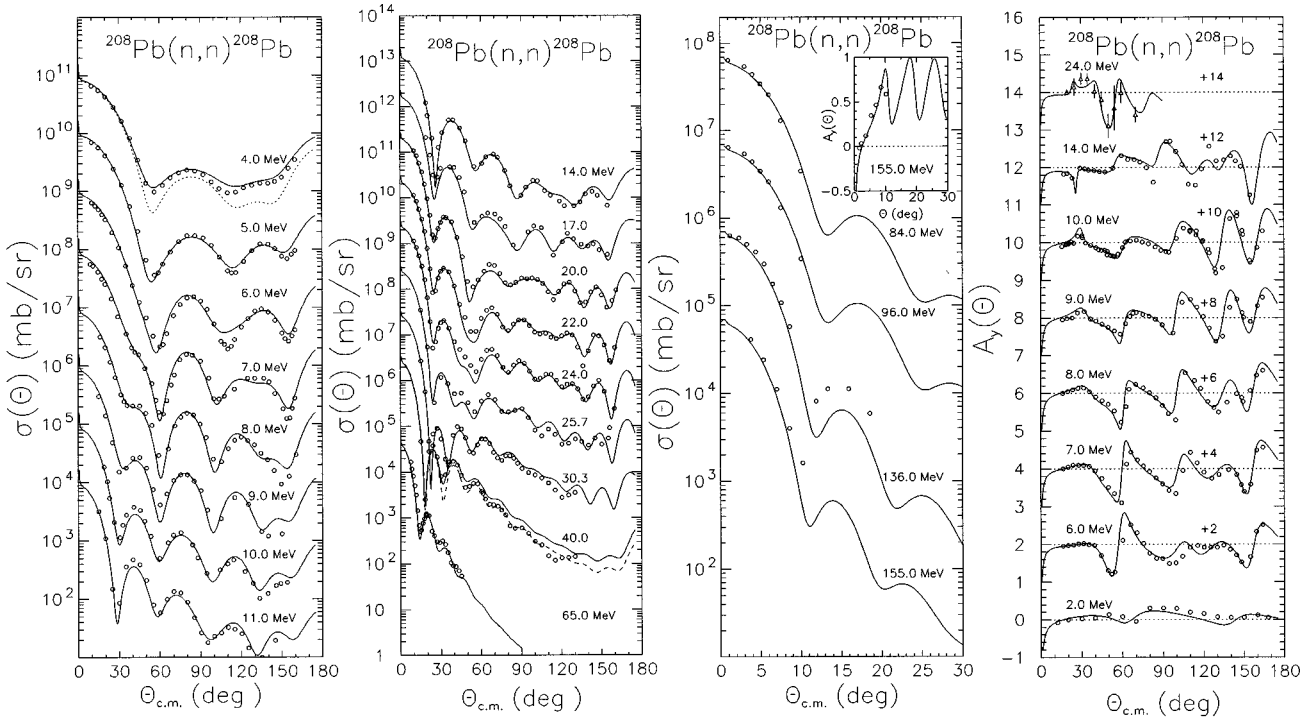

FIG. 15. Comparison of predicted differential cross sections and analyzing powers with experimental data, for neutrons scattered from ^{208}Pb between 2 MeV and 155 MeV. For more details, see the caption of Fig. 10.

B. $\vec{p}+X$ systems

1. ^{40}Ca target

For this light target of our sample the agreement between measured and calculated $\sigma(\theta)$ and $A_y(\theta)$ values is quite satisfactory although not as good as that obtained for neutron projectile. Figure 16 displays such a comparison. One clearly sees in this figure that the $\sigma(\theta)$ predictions around 20 MeV are slightly low for intermediate angles. In the vicinity of 40 MeV, the opposite trend is observed.

The agreement observed for $A_y(\theta)$ is also reasonably good for $\theta \leqslant 120°$ for incident energies up to 201 MeV. The spin rotation function $Q(\theta)$ measured at the high energy limit of our study is shown in Fig. 17 and compared with our OMP predictions (solid curve). $Q(\theta)$ is accurately accounted for at 201 MeV, especially if the best fit normalization parameters (differing from the global ones only by $\lambda_{w_{so}}$ here taken as $\lambda_{w_{so}} = -12$) are used (dashed curve). The spin rotation function $R(\theta)$ measured [179] at 65 MeV (Fig. 18) is also precisely accounted for by our global OMP using frozen parameters. Such an agreement between the experimental and calculated spin rotations functions is also observed for ^{58}Ni, ^{90}Zr, and ^{208}Pb and demonstrates the good predictive power of the potential used is this work. This agreement also demonstrates that, given good quality potentials, an OMP based on the Schrödinger equation can accurately predict the spin rotation parameters $Q(\theta)$ and $R(\theta)$ up to 201 MeV.

The reaction cross section (Fig. 19) is well described by the OMP model above 25 MeV where the difference between measured and calculated values does not exceed 10%. Below 20 MeV, this difference, which can reach 20%, is attributed to the presence of resonances that creep quite high in energy.

2. ^{56}Fe target

Figure 20 illustrates a comparison between measured and calculated $\sigma(\theta)$ and $A_y(\theta)$ angular distributions for ^{56}Fe. The overall agreement is as good as, or even better than that obtained for ^{40}Ca. Predictions and measurements for σ_R deviate by less than 10% (see Fig. 19).

3. ^{58}Ni target

The ^{58}Ni nucleus was deliberately excluded from the proton database used in Sec. V B to fix the proton normalization factors. Therefore we are able to offer blind $\sigma(\theta)$ and $A_y(\theta)$ predictions at many incident energies in Fig. 21. The agreement between data and OMP calculations is spectacular from the Coulomb barrier up to 200 MeV. We also accurately predict the the $R(\theta)$ variable (Fig. 18) at 65 MeV.

4. ^{63}Cu target

Since differential scattering measurements for ^{63}Cu are scarce, only σ_R has been considered. Final potential predictions for the reaction cross section are shown in Fig. 19 where they are compared with data for ^{63}Cu (larger symbols) and ^{nat}Cu (smaller symbols). The agreement is good.

5. ^{90}Zr target

The measured and calculated $\sigma(\theta)$ and $A_y(\theta)$ values are compared in Fig. 22 for ^{90}Zr. Good agreements are obtained, even at large angle where $\sigma(\theta)$ data is available for 135 MeV incident protons. Our model also accurately reproduces the measured $R(\theta)$'s at 65 MeV (Fig. 18). When extended to reaction cross sections (Fig. 19), this comparison shows that the OMP predictions are less than 10% away from the experimental values.

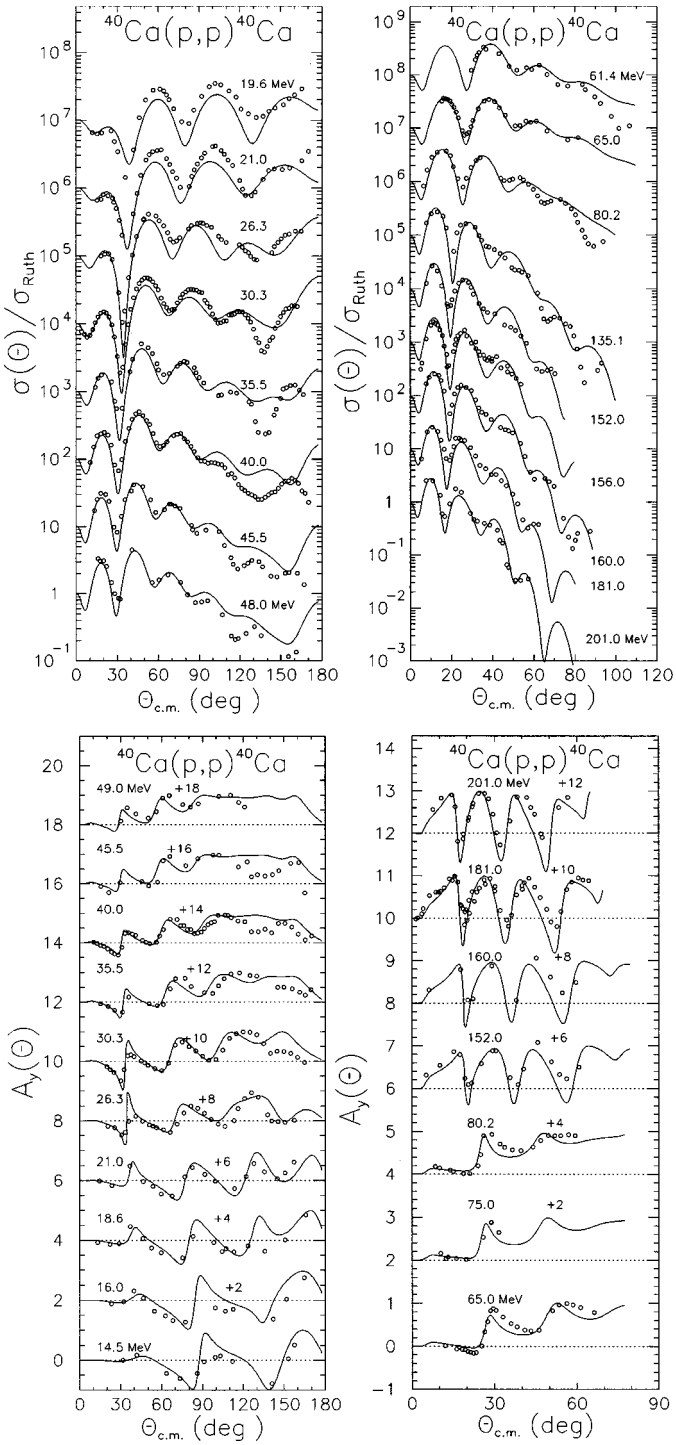

FIG. 16. Predicted scattering cross sections and analyzing powers (solid lines) compared with experimental data (open circles) for protons incident on ^{40}Ca between 14.6 MeV and 201 MeV. Note that elastic cross sections are presented as ratios to the Rutherford cross sections (σ_{Ruth}). These are offset by factors of 10, while the analyzing powers are shifted by 2.

6. ^{120}Sn target

The tin mass region has not been thoroughly covered in proton scattering studies up to 200 MeV. This is why we are unable to make a strong case of our semimicroscopic OMP predictive power in this instance. However the few $\sigma(\theta)$ and

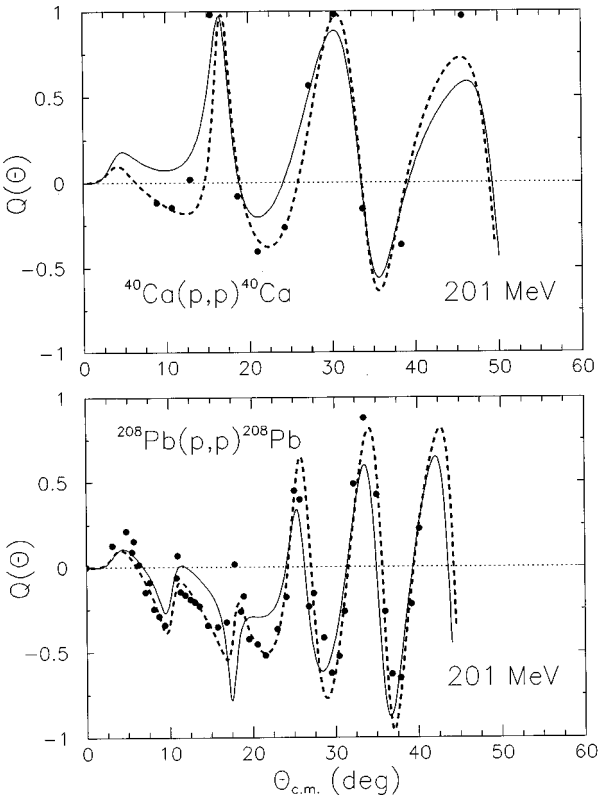

FIG. 17. Comparison of calculated spin rotation functions Q (lines) with the experimental data (solid dots) for 201 MeV protons incident on ^{40}Ca and ^{208}Pb. The solid lines represent the results of the calculations using our global OMP while the dashed lines are for calculations made using the best fit values of the normalization factors.

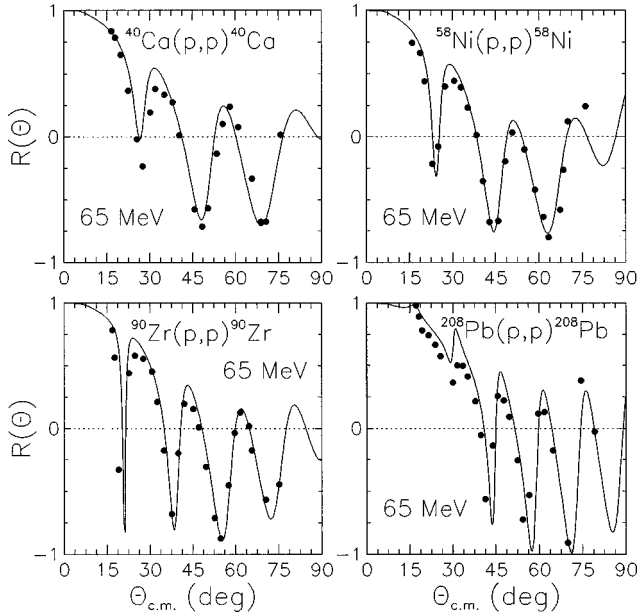

FIG. 18. Comparison of calculated spin rotation functions R (lines) with the experimental data (solid dots) [179] for 65 MeV protons incident on ^{40}Ca, ^{58}Ni, ^{90}Zr, and ^{208}Pb. The solid lines represent the results of the calculations using our global OMP.

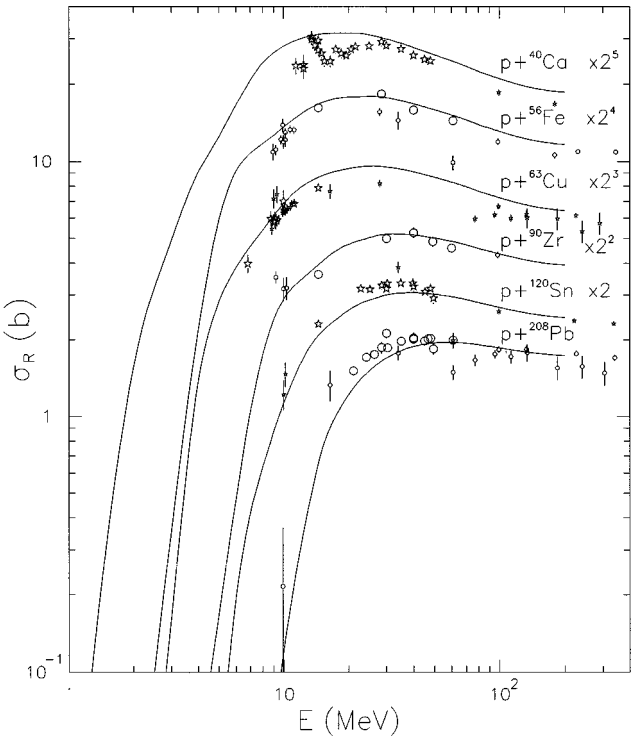

FIG. 19. Comparison between calculated (solid lines) and experimental reaction cross sections (open symbols), for protons incident on ^{40}Ca, ^{56}Fe, ^{63}Cu, ^{90}Zr, ^{120}Sn, and ^{208}Pb below 200 MeV. Larger symbols are for isotopic measurements and smaller ones are for elemental targets.

$A_y(\theta)$ measurements available for ^{120}Sn and ^{116}Sn indicate that our model predictions are accounting reasonably well for the available data (see Fig. 23). On the other hand, the measured and calculated σ_R values are in good agreement up to 200 MeV (Fig. 19).

7. ^{208}Pb target

^{208}Pb is the heaviest target nucleus in the set of proton nucleus scattering studies presented in this work. Many $\sigma(\theta)$ and $A_y(\theta)$ measurements spread over the 10–201 MeV range are available so that the $\vec{p}+^{208}$Pb system provides a stringent test for our OMP predictions. In Figs. 24 and 25, these predictions are shown to match very well the $\sigma(\theta)$ and $A_y(\theta)$ differential scattering measurements. This excellent agreement obtained here for incident protons and earlier for incident neutrons enhances our presumption that the LDA taken at the target coordinate is best suited for JLM model studies in the region of heavy spherical nuclei. OMP calculations for the spin rotation function Q are shown in Fig. 17 where they are compared with measurements at 201 MeV. The agreement is good. However, the $Q(\theta)$ predictions are improved and those for $\sigma(\theta)$ and $A_y(\theta)$ kept nearly as good by using (like for ^{40}Ca) the best fit values of the λ_i's (i.e., $\lambda_w=1.35$ and $\lambda_{w_{so}}=-12$). The $R(\theta)$ spin rotation function measured at 65 MeV (Fig. 18) is also well accounted for by our global OMP. Finally, Fig. 19 shows that the reaction cross section is reproduced with good accuracy between the Coulomb barrier and 200 MeV.

8. Other target nuclei

OMP analyses conducted for some target nuclei (^{54}Fe, ^{60}Ni, ^{93}Nb, and ^{209}Bi) are not shown here, but are available on request.

C. Remarks

Before closing this section, we would like to make a few comments. The first one deals with the σ_R data for which most measurements were performed in the early days of proton scattering and reaction studies; their accuracy is by far inferior to the 1% precision currently achieved in recent σ_T measurements performed at Los Alamos [33]. As a consequence, the available σ_R data has put weak constraints on our model parametrization. High precision σ_R measurements are needed to further challenge our predictions.

The second remark is related to the energy dependence of the calculated σ_R values. As can be seen in Fig. 19, these values, calculated at up to 10 MeV above the Coulomb barrier, get weaker as the target mass increases from $A=40$ to $A=208$. Since these features are not seen for the σ_T predictions in Fig. 9 our present comments on the σ_R predictions point to (i) the treatment of the Coulomb field in nuclear matter which may need modest improvements, or more likely (ii) the dispersion relations [180] which are not fully included in the JLM nuclear matter theory.

The third remark concerns the proton reactions at sub-Coulomb energies. σ_R predictions are shown in order to give an impression of their rapid drop as Z increases. This energy range deserves further work considering the important role it plays in astrophysics.

Our final comments deal with the complex spin-orbit potential. The Scheerbaum prescription adopted here leads to observable predictions of a quality which is beyond our early expectations. The meaning of this success remains to be explained on the basis of microscopic SO interactions.

D. Discussion

Volume integrals and root mean square radii are usually calculated for the purpose of comparing OMP predictions from separate analyses. Detailed comparisons between global parameters are here restricted to the case of protons incident on ^{40}Ca and ^{208}Pb.

We begin with the $\vec{p}+^{208}$Pb potential and we plot the volume integrals J_v/A, J_w/A [Fig. 26(a)], $J_{v_{so}}/A^{1/3}$, and $J_{w_{so}}/A^{1/3}$ [Fig. 26(b)] as well as rms radii R_{rms_v} ($R_{\mathrm{rms}_v}=\langle r_v^2\rangle^{1/2}$) and R_{rms_w} ($R_{\mathrm{rms}_w}=\langle r_w^2\rangle^{1/2}$) [Fig. 26(c)] of the present JLM potential components (solid curves). In these figures we also display (i) van Oers *et al.* best fit values [160] (open circles and triangles), and (ii) results from Fourier-Bessel analyses [181] (boxes). The datasets in Figs. 26(a) and 26(b) all agree within uncertainties. Our predicted rms radius [Fig. 26(c)] for the real central potential is satisfying since its values at low and high energies match the other datasets. The raise gradually showing up above 120 MeV reflects the evolution of $V(r)$ from volume to volume plus surface shape (see Fig. 1). Conversely, the imaginary potential changes from surface to volume shape as E in-

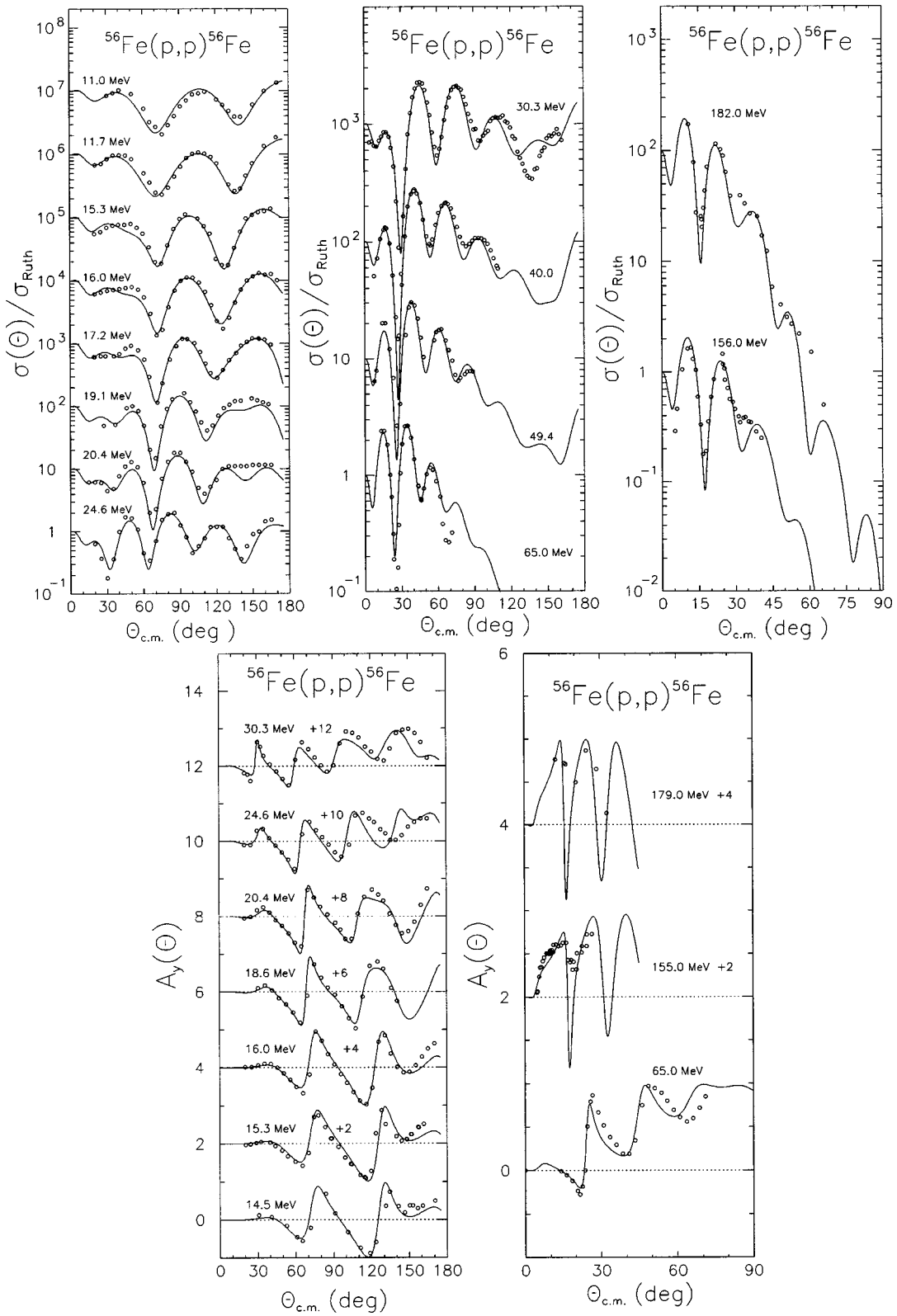

FIG. 20. Predicted scattering cross sections and analyzing powers (solid lines) compared with experimental data (open circles) for protons incident on ^{56}Fe between 11 MeV and 182 MeV. For more information see the caption of Fig. 16.

creases. As a consequence, its rms radius decreases. This pattern is followed by the present JLM OMP predictions and van Oers *et al.* data, but the two sets differ by approximately 10%.

All the predictions shown in Fig. 26(c) for the imaginary SO component support the view that its strength which is weak at low incident energy slowly increases with energy up to approximately 180 MeV. Although results for the real SO component display some dispersion around a smooth trend, the solid curve (our work) is consistent with the other symbols considering the uncertainties attached to the determination of this SO potential component.

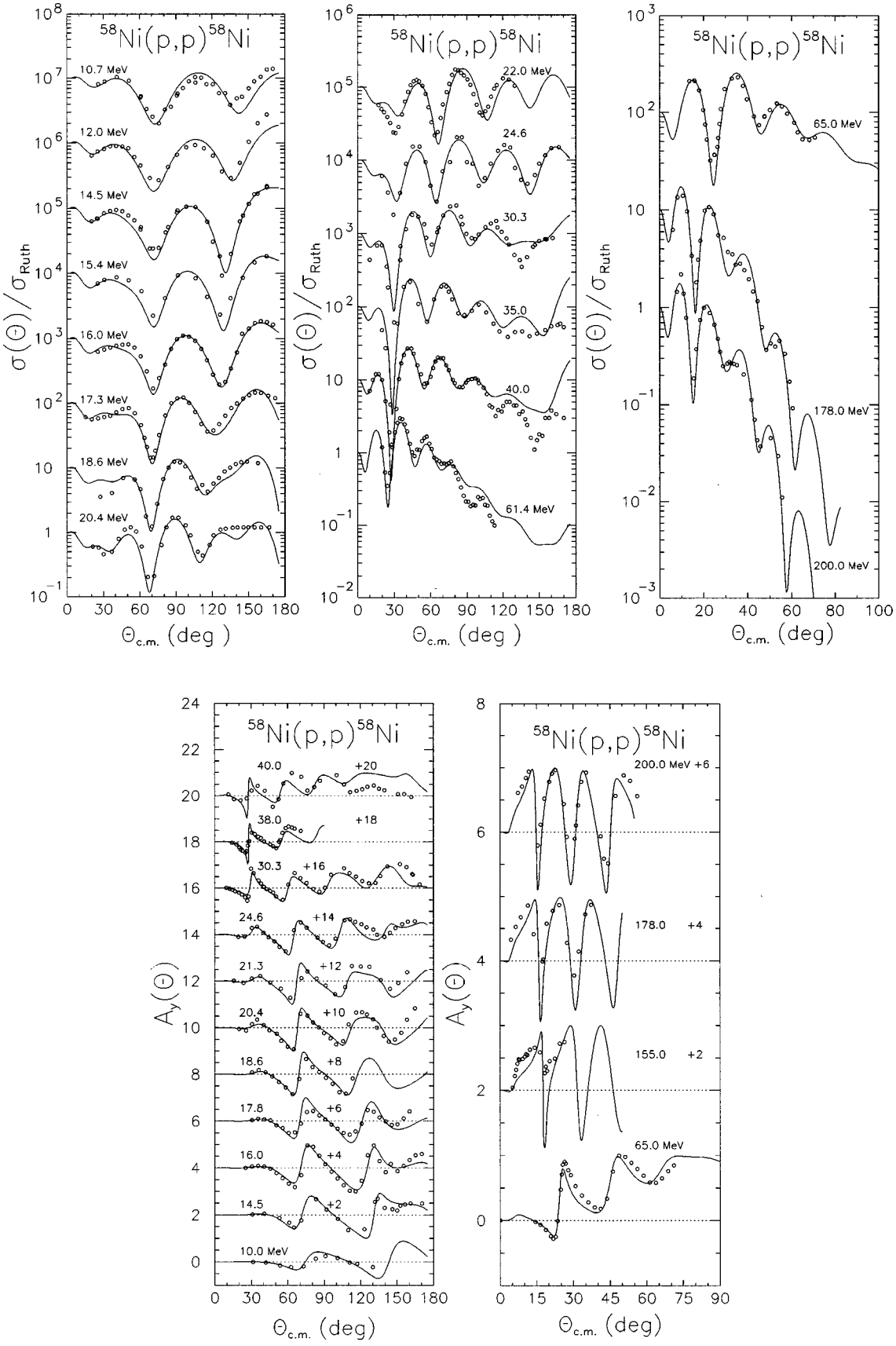

FIG. 21. Predicted scattering cross sections and analyzing powers (solid lines) compared with experimental data (open circles) for protons incident on ^{58}Ni between 10 MeV and 200 MeV. For more information see the caption of Fig. 16.

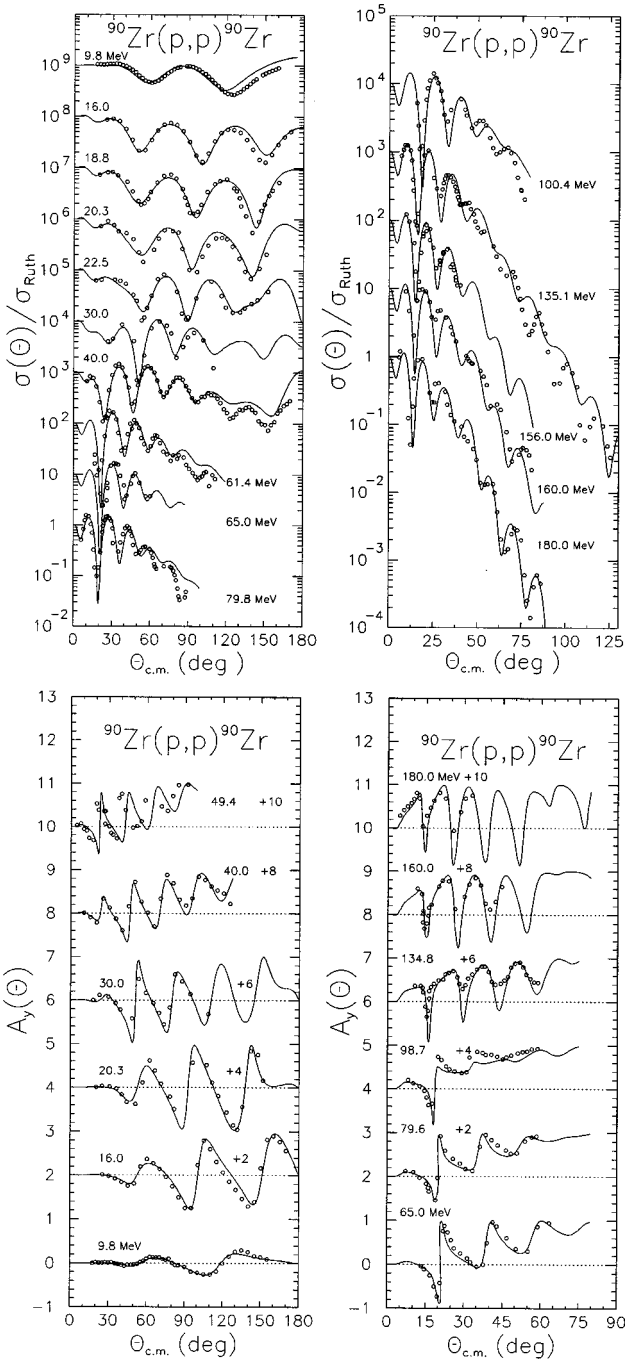

FIG. 22. Predicted scattering cross sections and analyzing powers (solid lines) compared with experimental data (open circles) for protons incident on ^{90}Zr between 9.8 MeV and 180 MeV. For more information see the caption of Fig. 16.

Similar comparisons are performed in Fig. 27 for the $\vec{p}+^{40}$Ca potential. Besides our predictions (solid curves), this figure also includes global parameters from (i) a dispersive OMP analysis [182] (dashed curves), (ii) standard OMP calculations [183] (open circles and triangles), (iii) Fourier-Bessel analyses [63] (boxes), and (iv) Dirac phenomenology [184] (solid circles and triangles). Except at 61 and 155 MeV, where some van Oers *et al.* results [183] fall apart from smooth patterns in energy, an overall good agreement exists between the various predictions including ours. Note that the rms radii deduced by van Oers *et al.* for the imaginary central potential are not plotted since they display erratic values which make any comparison with other datasets meaningless.

We also compare (but not display) our central potential rms radii with those of Nadasen *et al.* [120] and we find them in good agreement. However, if we compare the J_v/A and J_w/A values of the present work with those of Schwandt *et al.* [119], we find that although both datasets follow the same trends, they exhibit some noticeable quantitative differences. Such differences have been acknowledged in [119] and attributed to different radial shapes of the potentials. Note, however, that the volume integrals of the SO part of our potential are in good agreement with those of [119].

Lastly, we extend the discussion of the properties of the potential to radial shapes at 201 MeV. For the $\vec{p}+^{40}$Ca system, these distributions are shown in Fig. 28 (solid curves) where they are compared with the spread of values (shaded areas) deduced for several OMPs evaluated using different LDA prescriptions and effective interactions [26]. Present radial shapes of the complex central potential are well within the bounds of shaded areas. For the complex SO components, the agreement is not as good as that discussed above. However, we do not view this as a problem since Seifert *et al.* mention that the error bars shown in Fig. 21 of [26] are likely to be too small.

VII. SUMMARY

We have performed a large scale study of the semimicroscopic optical model potential built from nuclear matter by Jeukenne, Lejeune, and Mahaux. Our early motivation was to define the range of validity of this model in spherical OMP analyses conducted up to 200 MeV, for protons and neutrons incident on closed- and near closed-shell nuclei from ^{40}Ca to ^{209}Bi. Prior to performing these OMP analyses, we have established a new parametrization of the on-shell mass operator which extends the original JLM parametrization beyond 160 MeV.

Several prescriptions for the local density approximation have been tested, using radial densities obtained from self-consistent mean field (i.e., HFB) calculations based on Gogny's force. We got the best overall results by evaluating the LDA at the target nucleus coordinate. Performing optical model calculations up to 200 MeV also requires a complex spin-orbit interaction. We have treated this OMP component as a phenomenological potential, and found that the SO form factor established by Scheerbaum is suitable for OMP analyses over the energy range of present interest.

Once the HFB densities have been calculated for ^{40}Ca, ^{54,56}Fe, ^{58,60}Ni, ^{63,65}Cu, ^{90}Zr, ^{93}Nb, ^{116,120}Sn, ^{208}Pb, and ^{209}Bi, the main thrust was put on fitting many neutron and proton, scattering and reaction measured observables using grid search techniques. The normalization factors deduced in this manner for the real and imaginary components of the central and spin-orbit potentials take on values which exhibit smooth variations as functions of energy when plotted separately for incident protons and neutrons. Prompted by these results, the normalization factors λ_v, λ_w, $\lambda_{v_{so}}$, and $\lambda_{w_{so}}$ attached to our semimicroscopic potential depths have been given simple close forms. Except at low incident energies where sizable nuclear structure effects are seen, and are

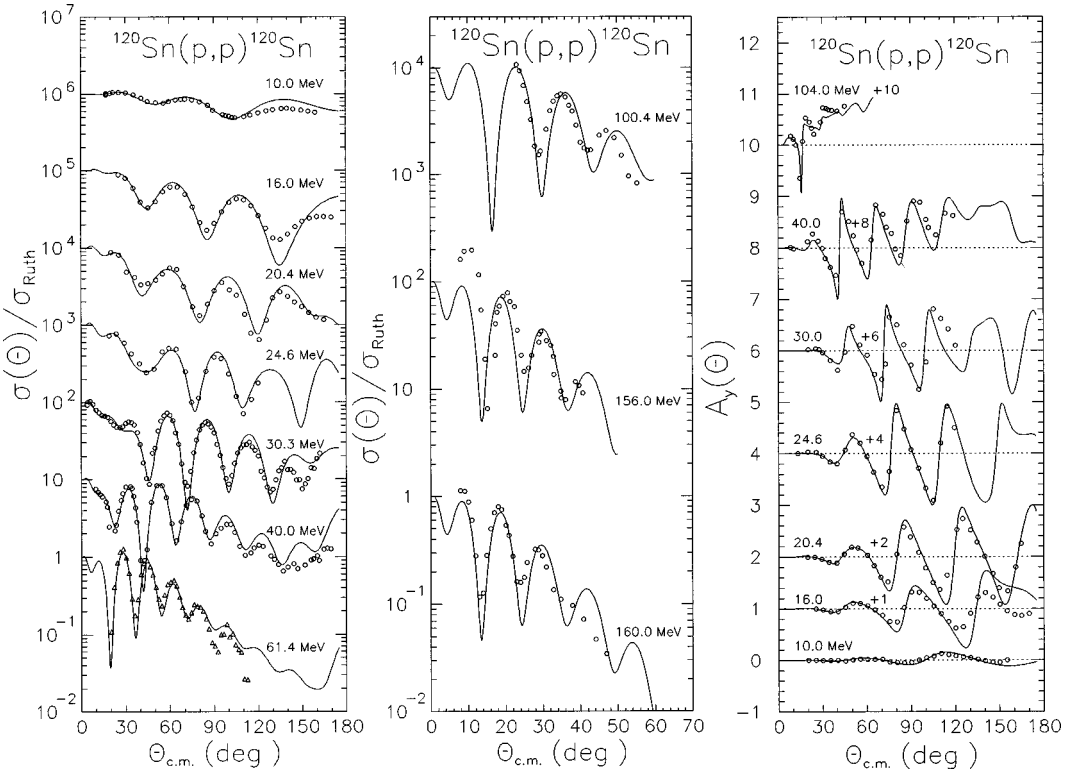

FIG. 23. Predicted scattering cross sections and analyzing powers (solid lines) compared with experimental data (open symbols) for protons incident on ^{116}Sn (triangles) and ^{120}Sn (circles) between 10 MeV and 160 MeV. For more information see the caption of Fig. 16.

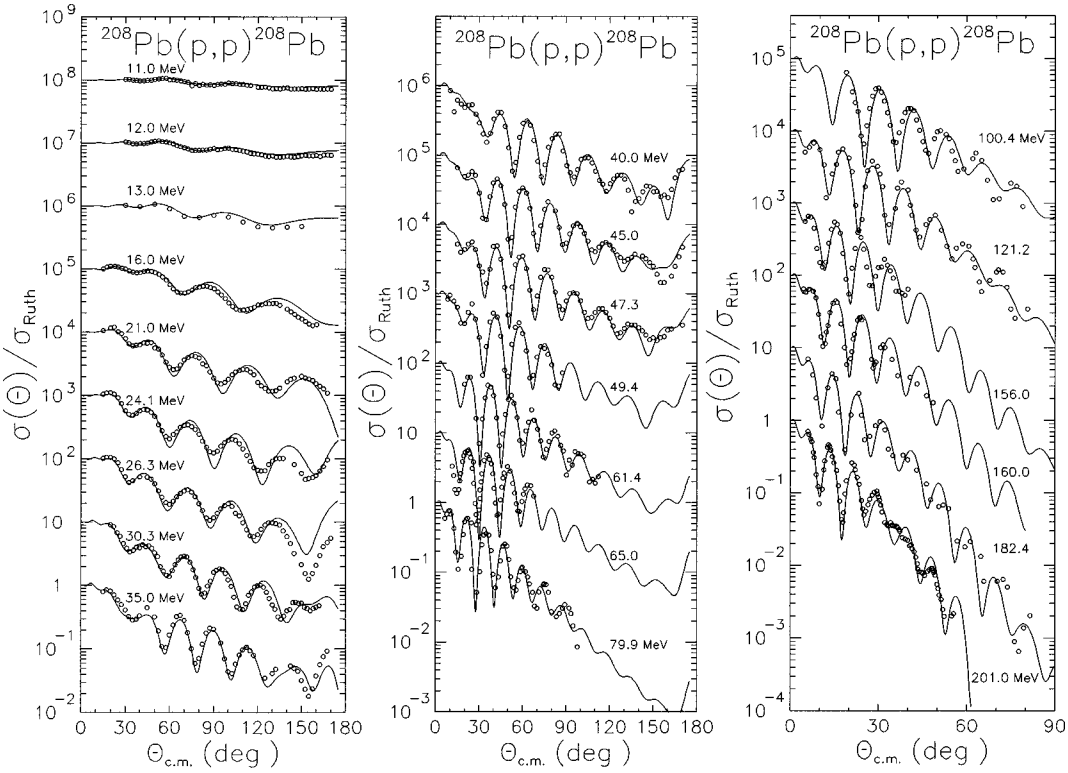

FIG. 24. Predicted scattering cross sections (solid lines) compared with experimental data (open circles) for protons incident on ^{208}Pb between 10 MeV and 201 MeV. For more information see the caption of Fig. 16.

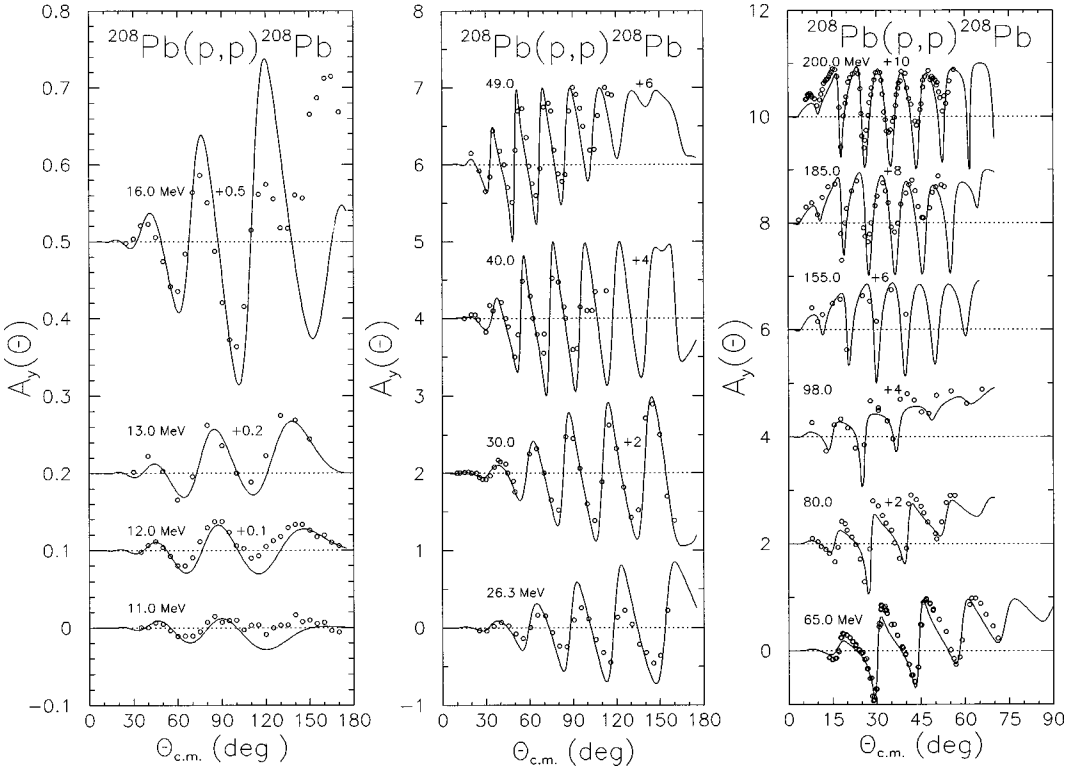

FIG. 25. Predicted analyzing powers (solid lines) compared with experimental data (open circles) for protons incident on ^{208}Pb between 11 MeV and 201 MeV. For more information see the caption of Fig. 16.

given a specific treatment, these close forms do not depend on the target mass as soon as $E \geqslant 10$ MeV. To our knowledge, this is the first time that a global semimicroscopic OMP built form nonrelativistic nuclear matter theory is established up to 200 MeV and for which the sole inputs are microscopic (HFB) densities. This potential, for which parameters are frozen, leads to OMP predictions which are in good overall agreement with scattering and reaction measurements analyzed above 1 MeV for incident neutrons, and above the Coulomb barrier for incident protons. At 200 MeV for the $\vec{p}+^{40}$Ca and $\vec{p}+^{208}$Pb systems, the agreement is as good as that obtained previously using other folding potentials with different LDA prescriptions. Moreover, the good

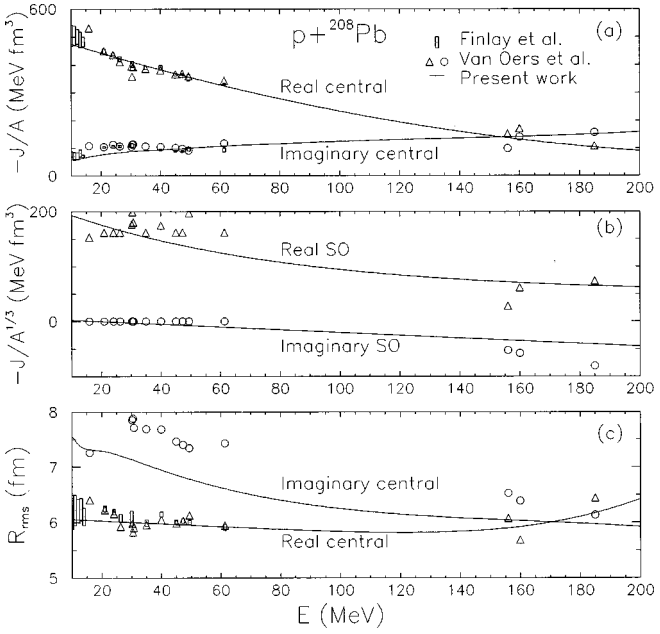

FIG. 26. Global properties of the $p+^{208}$Pb potential. (a) Volume integrals for the complex central term, (b) volume integrals for the complex SO term, and (c) rms radii for the complex central term. Solid lines represent the present calculations, and symbols are from separate works.

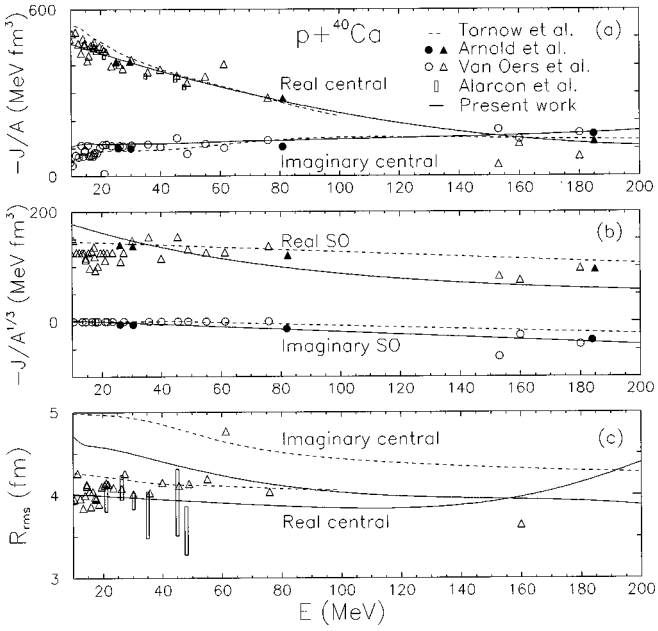

FIG. 27. Global properties of the $p+^{40}$Ca potential. For more details see the caption of Fig. 26.

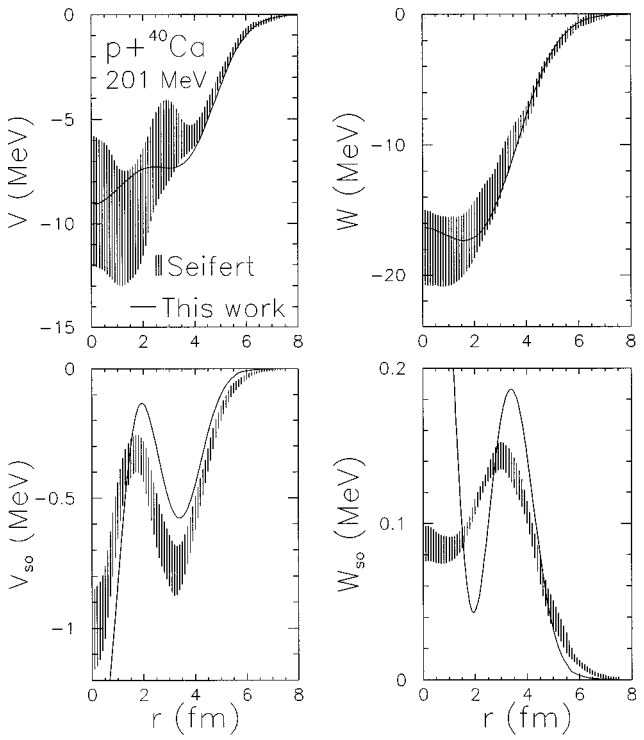

FIG. 28. Potential radial shape. Comparison between our global OMP (solid line) and the spread of several OMPs calculated using various effective interactions and LDA prescriptions (shaded area) for the system $p+{}^{40}$Ca at 201 MeV.

agreement between our calculations and spin rotation functions measured for several nuclei shows that, below 200 MeV, a scattering model based on the Schrödinger equation can be used to successfully predict the observables $Q(\theta)$ and $R(\theta)$, if a good quality potential is used. To our knowledge, this is the first time that such a success is achieved using a nonrelativistic OMP model calibrated on $\sigma(\theta)$ and $A_y(\theta)$ observables only.

Since our folding potential has not been designed and tested at higher incident energies, its range of validity is strictly limited to $E \leqslant 200$ MeV. We also wish to emphasize that our semimicroscopic OMP should not be used for scattering from stable, unstable, and halo nuclei with masses $A < 40$. Although we know from previous scattering studies on ^{9}Be [185], ^{13}C, and ^{16}O [10], and a few halo nuclei [186] that the local density approximation is a sound hypothesis, our limited experience gained for light nuclei clearly indicates that the present LDA is not an optimum for $A < 40$. In this respect, an extension of our work to target nuclei lighter than ^{40}Ca would be worth doing.

Notwithstanding the above limitations, the present model, that is free of adjustable parameter and rests upon microscopic foundations, has successfully passed a broad spectrum of tests, and therefore can be used for producing solid predictions.

By now, we are concentrating our efforts on (i) the $75 \leqslant A \leqslant 113$ region where the imaginary proton-nucleus potential is known to display an ''anomalous'' behavior at sub-Coulomb energies, and (ii) strongly deformed nuclei in the rare earth and actinide regions. Our preliminary results are encouraging. They also support the widespread view that reducing NM effective interactions to local potentials through a local density approximation is a reliable method in nucleon scattering and reaction studies.

ACKNOWLEDGMENTS

We wish to express our gratitude to Dr. F.S. Dietrich for providing a code used to calculate folding potentials, and to Dr. J. Raynal for his interest and endless effort upgrading the ECIS code. We are also indebted to Professor C. Mahaux for his major contributions in establishing the optical potential on microscopic grounds, without which the present analyses would not have been possible.

[1] *Microscopic Optical Potentials*, Proceedings of the Hamburg 1978 Conference, edited by H.V. von Geramb, Lecture Notes in Physics Vol. 89 (Springer-Verlag, Berlin, 1979).
[2] *The Interaction Between Medium Energy Nucleons in Nuclei*, Proceedings of the Workshop on the Interaction Between Medium Energy Nucleons in Nuclei, AIP Conf. Proc. No. 97, edited by H.O. Meyer (AIP, New York, 1982).
[3] J. Hufner and C. Mahaux, Ann. Phys. (N.Y.) **73**, 525 (1972).
[4] J.P. Jeukenne, A. Lejeune, and C. Mahaux, Phys. Rep., Phys. Lett. **25C**, 83 (1976).
[5] J.P. Jeukenne, A. Lejeune, and C. Mahaux, Phys. Rev. C **10**, 1391 (1974).
[6] J.P. Jeukenne, A. Lejeune, and C. Mahaux, Phys. Rev. C **15**, 10 (1977).
[7] A. Lejeune and P.E. Hodgson, Nucl. Phys. **A295**, 301 (1978).
[8] S. Mellema, R.W. Finlay, F.S. Dietrich, and F. Petrovich, Phys. Rev. C **28**, 2267 (1983).
[9] J.R.M. Annand, R.W. Finlay, and F.S. Dietrich, Nucl. Phys. **A443**, 249 (1985).
[10] J.S. Petler, M.S. Islam, R.W. Finlay, and F.S. Dietrich, Phys. Rev. C **32**, 673 (1985).
[11] L.F. Hansen, F.S. Dietrich, B.A. Pohl, C.H. Poppe, and C. Wong, Phys. Rev. C **31**, 111 (1985).
[12] F.A. Brieva and J.R. Rook, Nucl. Phys. **A291**, 299 (1977); **A291**, 317 (1977); **A297**, 206 (1977); **A307**, 493 (1978).
[13] H.V. von Geramb, in [2], p. 44.
[14] L. Rikus, K. Nakano, and H.V. von Geramb, Nucl. Phys. **A414**, 413 (1984).
[15] K. Nakayama and W.G. Love, Phys. Rev. C **38**, 51 (1988).
[16] L. Ray, Phys. Rev. C **41**, 2816 (1990).
[17] N. Yamaguchi, S. Nagata, and T. Matsuda, Prog. Theor. Phys. (Kyoto) **70**, 459 (1983).
[18] F. Petrovich, J.A. Carr, and H. McManus, Annu. Rev. Nucl. Part. Sci. **36**, 29 (1986).
[19] F. Petrovich, S.K. Yoon, M.J. Threapleton, R.J. Philpott, J.A. Carr, F.S. Dietrich, and L.F. Hansen, Nucl. Phys. **A563**, 387 (1993).
[20] L. Ray, G.W. Hoffmann, and W.R. Coker, Phys. Rep. **212**, 223 (1992).

[21] H.F. Arellano, F.A. Brieva, and W.G. Love, Phys. Rev. C **52**, 301 (1995); H.F. Arellano, F.A. Brieva, M. Sander, and H.V. von Geramb, *ibid.* **54**, 2570 (1996).
[22] C.R. Chinn, Ch. Elster, R.M. Thaler, and S.P. Weppner, Phys. Rev. C **51**, 1033 (1995); Ch. Elster, S.P. Weppner, and C.R. Chinn, *ibid.* **56**, 2080 (1997).
[23] R. Crespo, R.C. Johnson, and J.A. Tostevin, Phys. Rev. C **53**, 3022 (1996) and references therein.
[24] H.V. von Geramb, K. Amos, L. Berge, S. Bräutigam, H. Kohlhoff, and A. Ingemarsson, Phys. Rev. C **44**, 73 (1991); P.J. Dortmans and K. Amos, *ibid.* **49**, 1309 (1994); P.J. Dortmans, K. Amos, and S. Karataglidis, J. Phys. G **23**, 183 (1997) and references therein.
[25] J.J. Kelly *et al.*, Phys. Rev. C **44**, 2602 (1991) and references therein.
[26] H. Seifert *et al.*, Phys. Rev. C **47**, 1615 (1993) and references therein.
[27] C.D. Bowman *et al.*, Nucl. Instrum. Methods Phys. Res. A **320**, 336 (1992).
[28] C. Rubbia *et al.*, ''Conceptual design of a fast neutron operated high power energy amplifier,'' CERN Report No. CERN/AT/95-44(ET), 1995.
[29] S. Hama, B. Clark, E.D. Cooper, H.S. Sherif, and R.L. Mercer, Phys. Rev. C **41**, 2737 (1990).
[30] E.D. Cooper, S. Hama, B. Clark, and R.L. Mercer, Phys. Rev. C **47**, 297 (1993).
[31] R.W. Finlay, in *Proceedings of the Beijing International Symposium on Fast Neutron Physics*, edited by S. Zuxun, T. Hongqing, X. Jincheng, and Z. Jingshang (World Sientific, Singapore, 1992), p. 299.
[32] Yanhe Jin and R.W. Finlay, Phys. Rev. C **47**, 1697 (1993); R.W. Finlay, G. Fink, W. Abfalterer, P.W. Lisowski, G.L. Morgan, and R.C. Haight, in *Proceedings of the International Conference on Nuclear Data for Science and Technology*, edited by S. Quaim (Springer-Verlag, Berlin, 1992), p. 720.
[33] R.W. Finlay, W.P. Abfalterer, G. Fink, E. Montei, T. Adami, P.W. Liowski, G.L. Morgan, and R.C. Haight, Phys. Rev. C **47**, 237 (1993).
[34] R.W. Finlay and A.E Feldman, *Nucleon-Nucleus Optical Model up to 200 MeV*, Proceedings of a Specialists Meeting (OECD, Paris, 1997), p. 71.
[35] R. Kozack and D. Madland, Phys. Rev. C **39**, 1461 (1989).
[36] R. Kozack and D. Madland, Nucl. Phys. **A509**, 664 (1990).
[37] J.P. Jeukenne, A. Lejeune, and C. Mahaux, Phys. Rev. C **16**, 80 (1977).
[38] J.S. Bell and E.J. Squires, Phys. Rev. Lett. **3**, 96 (1959).
[39] R.V. Reid, Ann. Phys. (N.Y.) **50**, 525 (1972).
[40] K.A. Brueckner and J. Dabrowski, Phys. Rev. **134**, B722 (1964).
[41] J.W. Negele and K. Yazaki, Phys. Rev. Lett. **47**, 71 (1981).
[42] S. Fantoni, B.L. Friman, and V.R. Pandharipande, Phys. Lett. **104B**, 89 (1981).
[43] A. Lejeune, Phys. Rev. C **21**, 1107 (1980).
[44] H.V. von Geramb, F.A. Brieva, and J.R. Rook, in [2], p. 104.
[45] Ch. Lagrange and J.C. Brient, J. Phys. (Paris) **44**, (1983).
[46] Ch. Lagrange and A. Lejeune, Phys. Rev. C **25**, 2278 (1982).
[47] V. Gillet and J.M. Normand, Nucl. Phys. **A176**, 225 (1971).
[48] H.S. Camarda, F.S. Dietrich, and T.W. Phillips, Phys. Rev. C **39**, 1725 (1989).
[49] G. Bertch, J. Boryowicz, H. McManus, and W.G. Love, Nucl. Phys. **A284**, 399 (1977).
[50] R.R. Scheerbaum, Nucl. Phys. **A257**, 77 (1976).
[51] C.B. Dover and N. Van Giai, Nucl. Phys. **A190**, 373 (1972).
[52] J. Dechargé and D. Gogny, Phys. Rev. C **21**, 1568 (1980); J. Dechargé, L. Sips, and D. Gogny, Phys. Lett. **98B**, 229 (1981); J. Dechargé and L. Sips, Nucl. Phys. **A407**, 1 (1983).
[53] J.F. Berger, M. Girod, and D. Gogny, Comput. Phys. Commun. **63**, 365 (1990) and references therein.
[54] V.E. Starodubsky and N.M. Hintz, Phys. Rev. C **49**, 2118 (1994).
[55] B. Frois, J.B. Bellicard, J.M. Cavedon, M. Huet, P. Leconte, P. Ludeau, A. Nakada, Phan Zuan Ho, and I. Sick, Phys. Rev. Lett. **38**, 152 (1977).
[56] M. Girod and P.G. Reinhard, Nucl. Phys. **A384**, 179 (1982); B. Frois *et al.*, Phys. Lett. **122B**, 347 (1982); W. Boeglin *et al.*, Nucl. Phys. **A477**, 399 (1988); R.K.J. Sandor, H.P. Girod, M.N. Harakeh, C.W. de Jager, and H. de Vries, *ibid.* **A551**, 349 (1993); R.K.J. Sandor, H.P. Blok, M. Girod, M.N. Harakeh, C.W. de Jager, V.Yu. Ponomarev, and H. de Vries, *ibid.* **A551**, 378 (1993).
[57] B. Frois, C.N. Papanicolas, and S.E. Williamson, in *Modern Topics in Electron Scattering*, edited by B. Frois and I. Sick (World Scientific, Singapore, 1991), p. 352.
[58] J.D. Reber and J.D. Brandbenberger, Phys. Rev. **163**, 1077 (1967).
[59] W. Tornow, E. Woye, G. Mack, C.E. Floyd, K. Murphy, P.P. Guss, S.A. Wender, R.C. Byrd, R.L. Walter, T.B. Clegg, and H. Leeb, Nucl. Phys. **A385**, 373 (1982).
[60] D.E. Bainum, R.W. Finlay, J. Rapaport, J.D. Carlson, and W.G. Love, Phys. Rev. C **16**, 1377 (1977).
[61] G.M. Honoré, Ph.D. thesis, Duke University, 1986; G.M. Honoré, W. Tornow, C.R. Howell, R.S. Pedroni, R.C. Byrd, R.L. Walter, and J.P. Delaroche, Phys. Rev. C **33**, 1129 (1986).
[62] J. Rapaport, V. Kulkarni, and R.W. Finlay, Nucl. Phys. **A330**, 15 (1979).
[63] R. Alarcon, J. Rapaport, and R.W. Finlay, Nucl. Phys. **A462**, 413 (1987).
[64] N. Olsson, E. Ramstrom, and B. Trostell, Nucl. Phys. **A513**, 205 (1990).
[65] R.P. de Vito, S.M. Austin, W. Sterrenburg, and U.E.P. Berg, Phys. Rev. Lett. **47**, 628 (1981).
[66] R. Toepke, Ph.D. dissertation, Karlsruhe Kernforschungszentrum (1974).
[67] W.E. Kinney, ORNL Reports No. ORNL-TM-2052, 1968 and ORNL-4249, 1968.
[68] P. Boschung, J.T. Lindow, and E.F. Shrader, Nucl. Phys. **A161**, 593 (1971).
[69] J.P. Delaroche, S.M. El-Kadi, P.P. Guss, C.E. Floyd, and R.L. Walter, Nucl. Phys. **A390**, 541 (1982).
[70] T.P. Stuart, J.D. Anderson, and C. Wong, Phys. Rev. **125**, 276 (1962).
[71] S.M. El-Kadi, C.E. Nelson, F.O. Purser, R.L. Walter, A. Beyerle, C.R. Gould, and L.W. Seagondollar, Nucl. Phys. **A390**, 509 (1982).
[72] R.S. Pedroni, C.R. Howell, G.M. Honoré, H.G. Pfutzner, R.C. Byrd, R.L. Walter, and J.P. Delaroche, Phys. Rev. C **38**, 2052 (1988).
[73] C. Wong, J.D. Anderson, J.W. McClure, and B.D. Walker, Phys. Rev. **128**, 2339 (1962).
[74] E.L. Hjort, F.P. Brady, J.L. Romero, J.R. Drummond, D.S.

Sorenson, J.H. Osborne, B. McEachern, and L.F. Hansen, Phys. Rev. C **50**, 275 (1994).
[75] D.G. Foster, Jr. and D.W. Glasgow, Phys. Rev. C **3**, 576 (1971).
[76] F.G. Perey, T.A. Love, and W.E. Kinney, ORNL Report No. ORNL-4823, 1972.
[77] V. Culler and R.W. Waniek, Phys. Rev. **99**, 740 (1955).
[78] B. Ragent, UCRL Report No. UCRL-2337, 1953.
[79] D.C. Larson, J.A. Harvey, and N.W. Hill, ORNL Report No. ORNL-5787, 1981, p. 174.
[80] P.P. Guss, R.C. Byrd, C.E. Floyd, C.R. Howell, K. Murphy, G. Tungate, R.S. Pedroni, R.L. Walter, J.P. Delaroche, and T.B. Clegg, Nucl. Phys. **A438**, 187 (1985).
[81] Y. Yamamouti, J. Rapaport, S.M. Grimes, V. Kulkani, R.W. Finlay, D. Bainum, P. Grabmayr, and G. Randers-Pehrson, Proceedings of the International Conference on Nuclear Cross Sections for Technology, Knoxville (1979), p.146.
[82] W.E. Kinney and F.G. Perey, ORNL Report No. ORNL-4908, 1974.
[83] A. Bratentahl, S. Fernbach, R.H. Hildebrand, C.E. Leith, and J. Moyer, Phys. Rev. **77**, 597 (1950).
[84] G.L. Salmon, Nucl. Phys. **21**, 15 (1960).
[85] C.P. Van Zyl, R.G.P. Voss, and R. Wilson, Philos. Mag. **1**, 1003 (1956).
[86] R.S. Harding, Phys. Rev. **111**, 1164 (1958).
[87] C.E. Floyd, P.P. Guss, R.C. Byrd, K. Murphy, R.L. Walter, and J.P. Delaroche, Phys. Rev. C **28**, 1498 (1983).
[88] F.D. McDaniel, J.D. Brandberger, G.P. Glasgow, and H.G. Leighton, Phys. Rev. C **10**, 1087 (1974).
[89] P. Guenter, A.B. Smith, and J. Whalen, Phys. Rev. C **12**, 1797 (1975).
[90] R.W. Stooksberry, J.H. Anderson, and M. Goldsmith, Phys. Rev. C **13**, 1061 (1976).
[91] W. Tanaka, NEANDC Report No. NEANDC(J)-51/U, 1977, p. 11.
[92] J.P. Delaroche, Y. Wang, and J. Rapaport, Phys. Rev. C **39**, 391 (1989); Y. Wang and J. Rapaport, Nucl. Phys. **A517**, 301 (1990).
[93] D.E. Bainum, R.W. Finlay, J. Rapaport, H.H. Hadizadeh, and J.D. Carlson, Nucl. Phys. **A311**, 492 (1978).
[94] R.S. Pedroni, R.C. Byrd, G.M. Honoré, C.R. Howell, and R.L. Walker, Phys. Rev. C **43**, 2336 (1991).
[95] R.W. Harper, J.L. Weil, and J.D. Brandenberger, Phys. Rev. C **30**, 1454 (1984).
[96] R.W. Harper, Ph.D. thesis, University of Kentucky, Lexington, 1981.
[97] W. Tanaka, NEANDC Report No. NEANDC(J)-22/U, 1971, p. 10.
[98] P.P. Guss, R.C. Byrd, C.R. Howell, R.S. Pedroni, G. Tungate, R.L. Walter, and J.P. Delaroche, Phys. Rev. C **39**, 405 (1989).
[99] J. Rapaport, M. Mirzaa, H.H. Hadizadeh, D.E. Bainum, and R.W. Finlay, Nucl. Phys. **A341**, 56 (1980).
[100] W.P. Poenitz and J.F. Whalen, Argonne Natl. Lab. Report No ANL-NDM-80, 1983.
[101] V.M. Morozov, JU.G. Zubov, and N.S. Lebedeva, Jaderno-Fizicheskie Isseldovanija **A14**, 8 (1972).
[102] M.L. Roberts, P.D. Felsher, G.J. Weisel, Zemin Chen, C.R. Howel, W. Tornow, R.L. Walter, and D.J. Horen, Phys. Rev. C **44**, 2006 (1991) and references therein.
[103] J. Rapaport, T.S. Cheema, D.E. Bainum, R.W. Finlay, and J.D. Carlson, Nucl. Phys. **A296**, 95 (1978).
[104] R.W. Finlay, J.R.M. Annand, T.S. Cheema, J. Rapaport, and F.S. Dietrich, Phys. Rev. C **30**, 796 (1984).
[105] R.P. de Vito, Ph.D. thesis, Michigan State University, 1980.
[106] J.L. Fowler and E.C. Campbell, Phys. Rev. **127**, 2192 (1962).
[107] R.K. Das and R.W. Finlay, Phys. Rev. C **42**, 1013 (1990).
[108] L.F. Hansen, F.S. Dietrich, B.A. Pohl, C.H. Poppe, and C. Wong, Phys. Rev. C **31**, 111 (1985).
[109] E.T. Boschitz, R.W. Bercaw, and J.S. Vincent, Phys. Lett. **13**, 322 (1964).
[110] R.L. Varner, Ph.D. thesis, University of North Carolina at Chapel Hill, 1986; R.L. Varner, W.J. Thompson, T.L. McAbee, E.J. Ludwig, and T.B. Clegg, Phys. Rep. **201**, 57 (1991).
[111] H. Sakaguchi, M. Nakamura, K. Hatakana, A. Goto, T. Noro, F. Ohtani, H. Sakamoto, H. Ogawa, and S. Kobayashi, Phys. Rev. C **26**, 944 (1982).
[112] K.H. Bray, K.S. Jayaraman, G.A. Moss, W.T.H. van Oers, D.O. Wells, and Y.I. Wu, Nucl. Phys. **A167**, 57 (1971).
[113] D.L. Watson, J. Lowe, J.C. Dore, R.M. Craig, and D.J. Baugh, Nucl. Phys. **A92**, 193 (1967).
[114] B.W. Ridley and J.F. Turner, Nucl. Phys. **58**, 497 (1964).
[115] E.E. Gross, R.H. Bassel, L.N. Blumberg, B.J. Morton, A. van der Woude, and A. Zucker, Nucl. Phys. **A102**, 673 (1967).
[116] L.N. Blumberg, E.E. Gross, A. van der Woude, A. Zucker, and R.H. Bassel, Phys. Rev. **147**, 812 (1966).
[117] C.B. Fulmer, J.B. Ball, A. Scott, and M.L. Whiten, Phys. Rev. **181**, 1565 (1969).
[118] C. Rolland, B. Geoffrion, N. Marty, M. Morlet, B. Tatischeff, and A. Willis, Nucl. Phys. **80**, 625 (1966).
[119] P. Schwandt, H.O. Meyer, W.W. Jacobs, A.D. Bacher, S.E. Vidgor, M.D. Kaitchuck, and T.R. Donoghue, Phys. Rev. C **26**, 55 (1982).
[120] A. Nadasen, P. Schwandt, P.P. Singh, W.W. Jacobs, A.D. Bacher, P.T. Debevec, M.D. Kaitchuck, and J.T. Meek, Phys. Rev. C **23**, 1023 (1981).
[121] V. Comparat, R. Frascaria, N. Marty, M. Morlet, and A. Willis, Nucl. Phys. **A221**, 403 (1974).
[122] J. Stephenson, J. Phys. Soc. Jpn. (Suppl.) **55**, 316 (1985).
[123] W. Bauhoff, At. Data Nucl. Data Tables **35**, 429 (1986).
[124] J.F. Turner, B.W. Ridley, P.E. Cavanagh, G.A. Gard, and A.G. Hardacre, Nucl. Phys. **58**, 509 (1964).
[125] J. Beneviste, A.C. Mitchel, and A.C. Fulmer, Phys. Rev. **133**, B317 (1964).
[126] L. Rosen, J.G. Berry, A.S. Goldhaber, and E.H. Auerbach, Ann. Phys. (N.Y.) **34**, 96 (1965).
[127] J.P.M.G. Melssen, Ph.D. thesis, Technische Hogeschool Eindoven, 1978.
[128] I.E. Dayton and G. Schranck, Phys. Rev. **101**, 1358 (1956).
[129] P. Kossanyi-Demay, R. de Swiniarski, and C. Glashauser, Nucl. Phys. **A94**, 513 (1967).
[130] S.F. Eccles, H.F. Lutz, and V.A. Madsen, Phys. Rev. **141**, 1067 (1966).
[131] M.K. Brussel and J.H. Williams, Phys. Rev. **114**, 525 (1959).
[132] G.S. Mandi, D.T. Jones, and D. Jacques, Nucl. Phys. **A165**, 384 (1971).
[133] G.W. Greenless, C.H. Poppe, J.A. Sievers, and D.L. Watson, Phys. Rev. C **3**, 1231 (1971).
[134] L.L. Lee, Jr. and J.P. Schiffer, Phys. Rev. **134**, B765 (1945).
[135] R. Alphonce, A. Johansson, and G. Tibel, Nucl. Phys. **4**, 643 (1957).

[136] A. Johansson, G. Tibel, and P. Hillman, Nucl. Phys. **11**, 540 (1959).
[137] A. Johansson, U. Svanberg, and P.E. Hodgson, Ark. Fys. **19**, 541 (1961).
[138] S. Kobayashi, K. Matsuda, Y. Nagahara, Y. Oda, and N. Yamamuro, J. Phys. Soc. Jpn. **15**, 1151 (1960).
[139] N. Baron, R. Leonard, and D. Lind, Phys. Rev. **180**, 978 (1969).
[140] C.B. Fulmer, Phys. Rev. **125**, 631 (1962).
[141] T. Eliyakut-Roshko, R.H. McCamis, W.T.H. van Oers, R.F. Carlson, and A.J. Cox, Phys. Rev. C **51**, 1295 (1995).
[142] A. Ingemarsson, A. Johansson, and G. Tibel, Nucl. Phys. **A322**, 285 (1979).
[143] H. Sakaguchi *et al.*, RCPN Annual Report, 1993, p. 4.
[144] L. Rosen, J.E. Broley, Jr., and L. Stewart, Phys. Rev. **121**, 1423 (1961).
[145] C. Hu, H. Kikuchi, S. Kobayashi, K. Matsuda, Y. Hagahara, Y. Oda, N. Takano, M. Takeda, and T. Yamazaki, J. Phys. Soc. Jpn. **14**, 861 (1959).
[146] D.W. Dewins, H.H. Forester, and G.G. Gigas, Nucl. Phys. **35**, 617 (1962).
[147] C.F. Hwang, G. Clausnitzer, D.H. Nordby, S. Suwa, and J.H. Williams, Phys. Rev. **131**, 2602 (1963).
[148] W.S. Gray, R.A. Kenefick, J.J. Krausharr, G.R. Satchler, Phys. Rev. **142**, 142 (1966).
[149] J.B. Ball, C.B. Fulmer, and R.H. Bassel, Phys. Rev. **135**, B706 (1964).
[150] C. Glashauser, R. de Swiniarski, J. Goudergues, R.M. Lombard, B. Mayer, and J. Thirion, Phys. Rev. **184**, 1217 (1969).
[151] R. de Swiniarski *et al.*, Can. J. Phys. **55**, 43 (1977).
[152] K. Kwiatkowski and S. Wall, Nucl. Phys. **A301**, 349 (1978).
[153] S.D. Wassenaar, Ph.D. Thesis, Technische Hogeschool Eindoven, 1982.
[154] R.M. Craig, J.C. Dore, G.W. Greenless, J.S. Lilley, and J. Love, Nucl. Phys. **58**, 515 (1964).
[155] M.P. Fricke, E.E. Gross, B.J. Morton, and A. Zucker, Phys. Rev. **156**, 1207 (1967).
[156] P.G. Roos and N.S. Wall, Phys. Rev. **140**, B1237 (1965).
[157] R.F. Carlson, A.J. Cox, T. Eliyakut-Roshko, and W.T.H. van Oers, Can. J. Phys. **73**, 512 (1995).
[158] S.D. Wassenaar, P.J. van Hall, S.S. Klein, G.J. Nijgh, J.H. Polane, and O.J. Poppema, J. Phys. G **15**, 181 (1989).
[159] W. Kretscmer, M. Loh, K. Spitzer, and W. Stach, Phys. Lett. **87B**, 343 (1975).
[160] W.T.H. van Oers, Huang Haw, N.E. Davison, A. Ingemarsson, B. Fagerstrom, and G. Tibell, Phys. Rev. C **10**, 307 (1974).
[161] G.W. Greenless, V. Hnizdo, O. Karban, and J. Love, Phys. Rev. C **3**, 1063 (1970).
[162] D.A. Hutcheon *et al.*, in *Polarization Phenomena in Nuclear Physics-1980* Proceedings of the Fifth International Symposium on Polarization Phenomena in Nuclear Physics, Santa Fe, AIP Conf. Proc. No. 69, edited by G.G. Olsen, R.H. Brown, N. Jarnie, W.W. McNaughton, and G.M. Hale (AIP, New York, 1981), p. 454.
[163] M. Ju, M.S. thesis, Simon Fraser University, 1987.
[164] N. Ottenstein, S.J. Wallace, and J.A. Tijon, Phys. Rev. C **38**, 2272 (1988).
[165] S. Yamabe, M. Takeda, M. Kondo, S. Kato, T. Yamazaki, N. Takahashi, N. Kawai, and R. Chiba, J. Phys. Soc. Jpn. **17**, 729 (1962).
[166] F.S. Dietrich (private communication).
[167] J. Raynal, CEA Report No. CEA-N-2772, 1994.
[168] W. Hauser and H. Feshbach, Phys. Rev. **87**, 336 (1952).
[169] P.A. Moldauer, Nucl. Phys. **A344**, 185 (1980) and references therein.
[170] J. Schwinger, Phys. Rev. **73**, 407 (1948).
[171] W. Heckrotte, Phys. Rev. **101**, 1406 (1956).
[172] N. Alexander, K. Amos, and L. Berge, Aust. J. Phys. **47**, 681 (1994); **49**, 737 (1995); N. Alexander and K. Amos, *ibid.* **49**, 633 (1996).
[173] G.J. Weisel, W. Tornow, C.R. Howell, P.D. Flesher, M. AlOhali, M.L. Roberts, R.K. Das, R.L. Walter, and G. Mertens, Phys. Rev. C **54**, 1 (1996).
[174] S.F. Mughabghab, M. Divadeenam, and N.E. Holden, *Neutron Cross Sections* (Academic Press, New York, 1981).
[175] G. Passatore, Nucl. Phys. **A110**, 91 (1968).
[176] R.B. Firestone, *Table of Isotopes* (Wiley-Interscience, New York, 1996).
[177] F.S. Dietrich, R.W. Finlay, S. Mellema, G. Randers-Pehrson, and F. Petrovich, Phys. Rev. Lett. **51**, 1629 (1983).
[178] Y. Wang, C.C. Foster, R.D. Polak, J. Rapaport, and E.J. Stephenson, Phys. Rev. C **47**, 2677 (1993).
[179] H. Sakaguchi *et al.*, J. Phys. Soc. Jpn. (Suppl.) **55**, 61 (1986); M. Yosoi *et al.*, RCPN Annual Report, 1985, p. 4.
[180] C.C. Mahaux, H. Ngo, and G.R. Satchler, Nucl. Phys. **A449**, 354 (1986).
[181] R.W. Finlay, J. Wierzbicki, R.K. Das, and F.S. Dietrich, Phys. Rev. C **39**, 804 (1989).
[182] W. Tornow, Z.P. Chen, and J.P. Delaroche, Phys. Rev. C **42**, 693 (1990).
[183] W.T.H. van Oers, Phys. Rev. C **3**, 1550 (1971).
[184] L.G. Arnold *et al.*, Phys. Rev. C **25**, 936 (1982).
[185] J.J. Kelly *et al.*, Phys. Rev. C **46**, 711 (1992).
[186] M.D. Cortina-Gil *et al.*, Phys. Lett. B **401**, 9 (1997).